Redirection of SARS-CoV-2 to phagocytes by intranasal sACE2-Fc as a universal decoy confers complete prophylactic protection

Jingyi Wang[a]†, Jiangchuan Li[a]†, Alex W. Chin[b,c]†, Bin Luo[a,d], Junkang Wei[a], Jiale Qiu[a], Jianwei Ren[a,d], Yin Xia[a], Thomas Braun[a,e], Leo L.M. Poon[b,c,f]*, Bo Feng[a,d,g]*

[a] School of Biomedical Sciences, Faculty of Medicine; GIBH CAS-CUHK Joint Research Laboratory on Stem Cell and Regenerative Medicine, The Chinese University of Hong Kong; Hong Kong SAR, China.

[b] School of Public Health, LKS Faculty of Medicine, The University of Hong Kong; Hong Kong SAR, China.

[c] Centre for Immunology & Infection, Hong Kong Science and Technology Park; Hong Kong SAR, China.

[d] Centre for Regenerative Medicine and Health, Hong Kong Institute of Science & Innovation, Chinese Academy of Sciences; Hong Kong SAR, China.

[e] Department of Cardiac Development and Remodeling, Max-Planck-Institute for Heart and Lung Research, 61231, Bad Nauheim, Germany.

[f] HKU-Pasteur Research Pole, LKS Faculty of Medicine, The University of Hong Kong; Hong Kong SAR, China.

[g] Guangzhou Institutes of Biomedicine and Health, Chinese Academy of Sciences; Guangzhou 510530, China.

* Corresponding authors. Email: llmpoon@hku.hk (L.L.P.); fengbo@cuhk.edu.hk (B.F.).

† These authors contribute equally.

ABSTRACT

The rapid evolution of SARS-CoV-2 and other respiratory RNA viruses limits the success of current vaccines and antibody-based therapies. Engineered decoy receptors based on soluble angiotensin-converting enzyme 2 (sACE2) offer promising alternatives. Clinical-grade recombinant sACE2 inhibits SARS-CoV-2 replication *in vitro* but shows limited clinical success. This study reports an optimized sACE2 mutant fused to human IgG1 Fc (B5-D3), which redirects virus–decoy complexes to lysosomal degradation in macrophages. Intranasal prophylactic delivery of B5-D3 confers complete protection in SARS-CoV-2-infected K18-hACE2 mice. Abrogation of Fc effector functions compromises antiviral protection, indicating that Fc-mediated uptake of virus–decoy complexes is critical. Transcriptomic analysis suggests that B5-D3 induces early immune activation in lungs of infected mice. Bio-distribution and flow cytometry reveal selective targeting of airway phagocytes. *In vitro* assays confirm lysosomal degradation of virus–decoy complexes by macrophages without productive infection. These findings reveal a distinct antiviral mechanism via phagocytic clearance, supporting refined regimens for decoy treatments against SARS-CoV-2 and potentially other respiratory viruses.

KEYWORDS

sACE2-Fc, SARS-CoV-2, intranasal prophylaxis, Fc-mediated effector function, phagocytosis, decoy receptor

INTRODUCTION

47 The incessant evolution of severe acute respiratory syndrome coronavirus 2 (SARS-CoV-2)
48 and frequent breakthrough infections during the coronavirus disease 2019 (COVID-19)
49 pandemic underscore the critical need for effective antiviral strategies that are less susceptible
50 to immune escape than conventional vaccines and monoclonal antibody (mAb) therapies [44].

51 Soluble angiotensin-converting enzyme 2 (sACE2) therapies, which employ recombinant
52 forms of the human angiotensin-converting enzyme 2 (ACE2) receptor—the primary binding
53 site for the SARS-CoV-2 spike protein [15,24,32,34,44]—as viral decoys, have emerged as a
54 promising alternative [31]. However, an early clinical version (amino acid [aa] 1-740, APN01)
55 showed limited therapeutic benefit [51] and raised safety concerns about interference with
56 endogenous renin-angiotensin system (RAS) [36]. Subsequent protein engineering greatly
57 improved the pharmacological properties of sACE2, including fusion with a human IgG1 Fc
58 domain (sACE2-Fc) to enhance serum half-life [25], and mutagenesis to enhance spike-binding
59 affinity [4,11,33] and abolish enzymatic activity [11,26,33]. Potent sACE2-Fc mutants have
60 shown broad-spectrum neutralization against SARS-CoV-2 variants in animal models
61 [7,14,18]. However, the efficacy was limited. Despite the evidence suggesting a role for Fc-
62 mediated effector functions [7], underlying immune mechanisms remained poorly understood.
63 Further investigation is pivotal to advance the development of decoy-based antivirals and
64 harness their full potential.

65 In this study, we engineered and characterized a potent sACE2-Fc mutant (B5-D3) with just
66 two mutations that enhance spike-binding and eliminate enzymatic activity. Broad-spectrum
67 neutralization capacity was confirmed by *in vitro* neutralization assays. Markedly, stepwise
68 examinations of various administration routes and time points identified intranasal (IN)
69 prophylaxis as the most effective regimen for B5-D3, which conferred complete protection
70 against SARS-CoV-2 infection in K18-hACE2 mice across age groups. To understand how
71 sACE2-Fc decoys influence viral fate, we carried out systematic, mechanistic investigations

through transcriptomics, bio-distribution, and phagocytosis analysis. Our results revealed that IN-delivered B5-D3 engages airway phagocytes to promote early clearance and immune activation, which uncovers a distinct antiviral mechanism and offers new insights into the rational design of intranasal decoy-based interventions.

RESULTS

Engineered sACE2-Fc decoys with two single mutations achieve robust neutralization against SARS-CoV-2 variants

To enable an optimal performance of the ACE2 decoy, we adopted the established sACE2-Fc fusion design [25] (Fig. 1a; Supplementary Fig. 1) and examined selected combinations of mutations that enhance the binding of human ACE2 to SARS-CoV-2 spikes [4] (B2–B6) or abolish enzymatic activity [11,12,33] (A2, A3, D1–D5) (Supplementary Fig. 2a,b). Indeed, mutants B2–B6 showed enhanced neutralization capacity in pseudovirus-based neutralization assays [9] against both Wuhan-Hu-1 and D614G pseudoviruses [19] (Fig. 1b; Supplementary Fig. 2c, d). Among these, the single mutation T92Q (B5), which increases spike affinity by removing a critical glycosylation site at N90 [40], demonstrated neutralization enhancement comparable to other multi-mutants. Mutations within the catalytic domain (A2, A3, D1, D3, D4, D5, but not D2), whether alone or in combinations, had minimal effect on spike binding but effectively abolished enzymatic activity (Supplementary Fig. 2e). We next combined T92Q with each of the inactivating mutations. Notably, the resulting double mutants, namely B5-D1, B5-D3, B5-D4, B5-D5, all retained strong neutralization while lacking enzymatic function (Fig. 1b; Supplementary Fig. 3a-c). Among these, B5-D3 (T92Q/H374N) emerged as the top candidate (Fig. 1a, red stars; Fig. 1b, red arrow), exhibiting both functional efficacy and structural integrity, with minimal deviation from wild type (WT) ACE2 in structural modeling (root mean square deviation [RMSD] = 0.212 Å; Supplementary Fig. 3d) [1].

To assess the breadth of neutralization, we tested the double mutants against pseudoviruses bearing spikes from various variants of concern (VOCs) and variants of interest (VOIs) [3,10,13,17,30,44]. All constructs showed dose-dependent neutralization with higher potency than WT sACE2-Fc (Fig. 1c, d; Supplementary Fig. 4). We further examined B5-D3 using plaque reduction neutralization tests (PRNTs) in Vero E6 cells, which indeed, confirmed its robust activity against authentic Wuhan-Hu-1, Delta, and Omicron variants BA.5, BQ.1.22, and XBB.1.5 [2,30,44,45] (Fig. 1e-g). In contrast, Casirivimab, serving as positive control [46], showed efficacy only against early variants (Wuhan-Hu-1 and Delta; Fig. 1f), but failed to neutralize Omicron sublineages (Fig. 1g). These results demonstrate that a rationally engineered sACE2-Fc decoy with only two mutations could achieve potent and safe neutralization across SARS-CoV-2 variants, reducing the potential risks associated with extensive mutagenesis.

Prophylactic administration of the sACE2-Fc B5-D3 mutant via the intranasal route exhibits superior protection against SARS-CoV-2

Next, we evaluated the *in vivo* efficacy of the sACE2-Fc double mutant B5-D3 against SARS-CoV-2 infection using aged K18-hACE2 mice (10 – 12 months old) (Fig. 2a). 6 hours (h) before inoculating with 1×10^4 plaque-forming unit (PFU) of SARS-CoV-2 (Wuhan-Hu-1 strain), mice received a prophylactic dose of recombinant B5-D3 protein either intranasally (IN, 2.5 mg/kg) or intravenously (IV, 15 mg/kg). To simulate a therapeutic intervention, an additional group received IV B5-D3 (15 mg/kg) 24 h post-virus inoculation. The vehicle control group received an intranasal PBS dose 6 h before viral challenge. Over a 14-day observation period, all mice in the PBS group exhibited significant weight loss and succumbed to infection by 7 days post-infection (dpi) (Fig. 2b, c, black lines). Both IV-treated groups exhibited initial weight loss similar to the PBS group; however, two out of four mice in each

group began to regain weight from 10 dpi and survived until the observation endpoint (green and blue lines). Notably, all mice in the IN-prophylaxis group, despite receiving a 6-fold lower dose of B5-D3 protein, maintained stable body weight and achieved complete survival over the 14-day period (red lines).

To monitor viral burden, one mouse from each group was sacrificed at 4 dpi (Fig. 2a). No infectious viral particles were detected in lung homogenate from the IN-prophylaxis mouse. In contrast, mice treated with IV prophylaxis or therapy showed reduced but still detectable viral titers compared to the PBS group (Fig. 2d). Immunohistochemistry (IHC) staining further confirmed the absence of viral nucleocapsid (N) protein in the IN-treated mouse, whereas IV-treated mice showed residual infection and immune cell infiltration. Hematoxylin and eosin (H&E) staining revealed varying degrees of alveolar thickening in all mice (Fig. 2e).

To further explore the timing of IN administration, we treated a younger cohort of K18-hACE2 mice (2 – 3 months old) with B5-D3 (IN, 2.5 mg/kg) at –24 h, –6 h, or +24 h relative to viral challenge (Fig. 2f). Similarly, the PBS group exhibited substantial weight reduction from 4 dpi and reached approximately 20% loss by 7 dpi (Fig. 2g, black lines). Despite this, two of the five infected young mice eventually recovered, resulting in 40% survival (Fig. 2g, h, black lines). Interestingly, both the –24 h and –6 h IN prophylaxis groups maintained stable body weights (Fig. 2g, pink and red lines), resulting in survival rates of 80% and 100%, respectively (Fig. 2h). In contrast, the +24 h group showed substantial weight loss and no survival improvement compared to the PBS group, indicating limited therapeutic benefit when IN B5-D3 was administered post-infection (Fig. 2g, h, orange lines). Consistently, virus-neutralizing antibodies were detected in surviving mice from the PBS and +24 h groups at 14 dpi, indicating active infection and subsequent immune response. Whereas antibody levels remained minimal in the two IN-prophylaxis groups, suggesting effective prevention of viral replication (Fig. 2i).

147

148 **Efficient protection against SARS-CoV-2 by intranasal B5-D3 prophylaxis depends on**
149 **Fc-mediated effector functions**

150 Prompted by the significant protection conferred by IN prophylaxis with B5-D3, we examined
151 the early responses following SARS-CoV-2 challenge in K18-hACE2 mice. A new cohort of 2-
152 to 3-month-old mice received B5-D3 IN treatment 6 h before infection (–6 h), and lung tissues
153 were harvested at 1, 2, and 4 dpi for analysis (Fig. 3a). An additional group was treated with a
154 modified version of B5-D3, which contains L234A/L235A mutations in the human IgG1 Fc
155 region (B5-D3-LALA) to abrogate Fc effector functions [28] (Supplementary Fig. 5).
156 Quantitative PCR of viral spike (*S*) and nucleocapsid (*N*) RNA in lung tissues revealed only
157 marginal viral loads in the B5-D3-treated mice as early as 1 dpi, indicating efficient
158 suppression of early viral replication compared to the PBS group (Fig. 3b). Analysis of
159 infectious viral particles in lung homogenates further corroborated these observations,
160 demonstrating minimal or undetectable viral titers in the B5-D3 group at all time points (Fig.
161 3c). In contrast, PBS-treated mice exhibited consistently high viral loads. Interestingly, the B5-
162 D3-LALA group displayed varied outcomes, with significant viral burdens observed in two out
163 of three mice, indicating that Fc effector functions are critical for B5-D3-mediated protection
164 (Fig. 3b, c, right panels). Consistently, IHC staining for N protein in lung sections confirmed
165 the absence of viral infection in the B5-D3 group at all time points. Whereas signs of viral
166 replication were evident in the lungs of mice treated with PBS at as early as 1 dpi and in the
167 B5-D3-LALA-treated cohort by 4 dpi (Fig. 3d; Supplementary Fig. 6, left panels). Despite
168 variations in viral burden, H&E staining indicated alveolar thickening in all groups.
169 Particularly, the alveolar changes observed in the absence of detectable infection in B5-D3–
170 treated mice suggested immune activation without viral replication (Fig. 3e; Supplementary
171 Fig. 6, right panels). These findings demonstrated that IN prophylaxis with B5-D3 blocks

172 SARS-CoV-2 infection not only by neutralization but also by immune mechanisms such as Fc-
173 mediated effector functions.

174

175 **RNA-Seq analysis of lung transcriptomes reveals early antigen presentation and prompt**
176 **viral clearance following SARS-CoV-2 neutralization by B5-D3**

177 To delineate the immune mechanisms underlying B5-D3-mediated prophylactic protection
178 against SARS-CoV-2, we examined the transcriptomes of lung samples collected at 1, 2, and 4
179 dpi from the above experiment (Fig. 4a-d; Supplementary Fig. 7a). Unsupervised clustering
180 based on Pearson correlation distinguished samples with severe infection (mainly PBS-treated)
181 from those with subtle or no infection (mocks and most decoy-treated mice) (Supplementary
182 Fig. 7a). Corroborating the levels of viral infections observed, differential gene expression
183 (DGE) analysis revealed extensive inflammatory responses in the PBS groups, significantly
184 greater than in mock treatments. At 1, 2, and 4 dpi, 26, 1232, and 1756 genes were
185 upregulated, respectively, and were significantly enriched in Gene Ontology Biological Process
186 (GOBP) terms related to antiviral responses such as type I interferon (IFN) responses and
187 innate immune responses (Fig. 4a, b; Supplementary Fig. 7b-d) [47]. In stark contrast, DGE
188 analysis between B5-D3 prophylaxis and mocks at 1, 2, and 4 dpi showed subtle changes, with
189 only 1, 7, and 32 genes upregulated, respectively, and only moderate enrichment in
190 chemotaxis-related pathways at 4 dpi (Fig. 4c; Supplementary Fig. 7e). The B5-D3-LALA
191 group, however, had 264 genes upregulated at 4 dpi compared to the mocks, suggesting
192 incomplete protection and ongoing viral activity (Fig. 4d; Supplementary Fig. 7f).

193 To capture the immune activations specifically linked to B5-D3-triggered antiviral efficacy
194 other than infection-induced inflammation, we directly compared the B5-D3 and PBS groups
195 (Fig. 4e-j; Supplementary Fig. 8, 9). Interestingly, at 1 dpi, the B5-D3 group exhibited
196 enhanced expression of several immune-related genes, including *Lef1* [37], *Fscn1* [49], *Kcne4*

197 [8], *Tcrb*, and *Ccl22* [20,35], which are associated with early dendritic cell function and T cell
198 activation (Fig. 4e). Gene Set Enrichment Analysis (GSEA) of GOBPs and Kyoto
199 Encyclopedia of Genes and Genomes (KEGG) pathways further supported these findings.
200 Chemotaxis and pathways related to antigen presentation such as Rap1 signaling pathway [16]
201 and Th1 and Th2 cell differentiation were significantly activated in the B5-D3 group at 1 dpi
202 compared to PBS group (Fig. 4h-j; Supplementary Fig. 8a-c). Moreover, the B5-D3 groups
203 showed enhancement in cilium movement and metabolism of xenobiotics at both 2 and 4 dpi,
204 suggesting active clearance of viral particles due to effective early responses (Supplementary
205 Fig. 9c-f).

206 Furthermore, we collectively examined the GOBPs that were significantly activated in B5-D3
207 groups at either 1, 2, and 4 dpi among all treatment groups and time points. Markedly, B5-D3
208 group showed higher normalized enrichment scores (NES) in chemotaxis-related GOBP
209 pathways than PBS group at 1 dpi (Fig. 4k, purple boxes), while direct comparison between
210 B5-D3 and PBS groups further revealed the broad involvement of multiple types of effector
211 immune cells (Fig. 4l, purple box). These results collectively indicate that early immune
212 activation is a hallmark of B5-D3-mediated protection.

213 Finally, the lung transcriptomes from mice receiving B5-D3 without viral inoculation showed
214 high similarity to the PBS vehicle controls (Supplementary Fig. 10a). The 10 upregulated
215 genes identified showed poor correlation with the virus-inoculated B5-D3 group
216 (Supplementary Fig. 10b, c), supporting that early immune responses observed in B5-D3 IN
217 prophylaxis groups were primarily triggered by virus neutralization rather than by B5-D3
218 alone.

219

220 **Intranasally delivered B5-D3 is enriched in the respiratory tract and targets mainly the**
221 **airway macrophages**

222 The superior antiviral effects of IN over IV administration of B5-D3 as observed in the K18-
223 hACE2 infection experiments suggested the importance of mobilizing the local immunity
224 within the respiratory tract. To track IN B5-D3, we labeled B5-D3 protein with Alexa Fluor
225 750 (AF750) and examined its bio-distribution and kinetics after IN administration (Fig. 5a). *In*
226 *vivo* imaging showed that fluorescence-labeled B5-D3 (B5-D3-AF750) was present in the nasal
227 cavities for at least 24 h after a single IN dose in K18-hACE2 mice (Fig. 5b). *Ex vivo* images
228 further revealed that B5-D3-AF750 distributed in the respiratory tract from nasal cavity to lung
229 within 20 min and remained enriched in lungs by 24 h after administration (Fig. 5c). In
230 contrast, non-respiratory organs showed minimal signals, which were merely detectable in
231 urinary system and liver (Fig. 5d).

232 To further identify the immune cells in the respiratory tract that are actively engaged with IN
233 B5-D3, we performed flow cytometry analysis on bronchoalveolar lavage fluid (BALF) at 6 h
234 after IN administration of B5-D3-AF750 (Fig. 5e; Supplementary Fig. 11a). Corroborating
235 previous findings, over 95% of live BALF cells were $CD45^+$ immune cells, predominantly
236 $CD11c^+$Siglec-F^+ resident alveolar macrophages (AMs) in both treatment and vehicle groups
237 (Fig. 5f; Supplementary Fig. 11b). Notably, the IN administered B5-D3-AF750 was actively
238 retained in the $CD45^+$ cells, with positive rates exceeding 65% in all treated mice (Fig. 5g).
239 Among the $CD45^+$B5-$D3^+$ cells, more than 95% were macrophages, composed primarily of
240 $CD11c^+$Siglec-F^+ AMs (87.2 – 91.7%) and Siglec-$F^-$$CD11b^-$$F4/80^+$ monocyte-derived
241 macrophages (mono-Macs; 6.6 – 9.9%) (Fig. 5h, red arrows). Consistently, these macrophage
242 populations also exhibited the highest B5-D3 positive rates (Fig. 5i, j; Supplementary Fig. 12)
243 and greatest median fluorescent intensities (MFI) (Fig. 5k, red arrows) among all immune cell
244 types in the BALF, indicating the strongest B5-D3-AF750 uptake. Other phagocytic cell types
245 such as the type 2 conventional dendritic cells (cDC2) and monocytes also exhibited
246 considerable AF750 intensities (Fig. 5k, blue arrows; Supplementary Fig. 12b, c), suggesting

247 potential relationships between B5-D3 uptake and phagocytic activities. Confocal microscopy
248 of BALF cells after immunostaining further confirmed that the B5-D3-AF750 were present in
249 the cytoplasm after being retained in AMs (Fig. 5l). Together, these results demonstrate that
250 intranasal B5-D3 preferentially accumulates in the respiratory tract and is predominantly taken
251 up by airway macrophages, supporting their important role in mediating early immune
252 responses.

253

254 **sACE2-Fc facilitates phagocytosis of SARS-CoV-2 pseudovirus via mechanisms distinct**
255 **from ACE2-dependent viral infection**

256 To examine the implication of macrophage involvement in the early immune activation
257 observed in IN B5-D3 treatment groups, we performed cellular analysis using THP-1 cells as
258 an *in vitro* model for phagocytes [5] and examined the sACE2-Fc-dependent phagocytosis of
259 spike-pseudotyped lentiviruses. Indeed, immunostaining of HIV capsid protein p24 confirmed
260 the attachment and entry of pseudoviruses in the THP-1 cells in a B5-D3-dependent manner,
261 with an evidenced signal peak at 6 h post-co-incubation (Supplementary Fig. 13). Interestingly,
262 analysis on the THP-1-derived M0 and M1 macrophages detected even greater p24 signals,
263 indicating stronger phagocytosis activities compared to undifferentiated THP-1 cells (Fig. 6a,
264 b; Supplementary Fig. 14a, b, d, e). This process resembled antibody-dependent cellular
265 phagocytosis (ADCP), which was significant in THP-1-derived M0 and M1 macrophages [42].
266 Consistently, further examination revealed colocalization of internalized pseudovirus with
267 lysosomal associated membrane protein 1 (LAMP1), suggesting trafficking to lysosomes for
268 degradation [41] (Fig. 6c; Supplementary Fig. 14c, f).

269 We further compared this finding with the pseudovirus uptake in Calu-3 cells overexpressing
270 human ACE2 (hACE2-Calu-3; Supplementary Fig. 15) as a model of lung epithelial cells.
271 Distinctly, co-incubation with B5-D3 significantly reduced the pseudovirus entry in hACE2-

Calu-3 (Fig. 6d-f). Interestingly, despite the evident pseudovirus uptake facilitated by B5-D3 in the THP-1 and derivative macrophages, there was no correspondingly detectable luciferase activity in these cells, which indicates viral degradation within phagolysosomes instead of viral genome release or transgene expression (Fig. 6g). Corroborating these observations, western blot analysis showed absence of cleaved S2′ fragments in sACE2-Fc-treated macrophages, supporting that the pseudoviruses did not undergo membrane fusion or cytosolic release following uptake [50] (Fig. 6h). Collectively, these findings suggest that IN B5-D3 not only blocks viral entry into epithelial cells but also actively redirects SARS-CoV-2 to phagocytic clearance by engaging airway phagocytes via Fc-dependent mechanisms. Moreover, such ADCP-like process likely contributes to early immune activation and restricts the infection at the respiratory mucosal surface.

DISCUSSION

In this study, we comprehensively evaluated the protective efficacy and mechanistic basis of an optimized sACE2-Fc decoy (B5-D3) against SARS-CoV-2 infection. By introducing only two mutations (T92Q and H374N), we generated a minimally engineered sACE2-Fc mutant (B5-D3) that achieved broad-spectrum neutralization with minimal risk of disrupting the RAS. Among various administration routes and dosing schedules examined, we demonstrated that IN prophylaxis of B5-D3 achieved the most robust protection, completely preventing disease in both young and aged K18-hACE2 mice. Transcriptomics analysis of the infected lung samples at early time points revealed distinct IN B5-D3-dependent immune activation at the onset of infection, indicating B5-D3 acted not only as a viral decoy but also as an immune modulator. Corroborating these findings, bio-distribution analysis of fluorescence-labeled B5-D3 demonstrated rapid uptake and high accumulation in the respiratory tract, primarily within airway macrophages. Furthermore, phagocytosis assays supported that sACE2-Fc decoy

297 mediated a rapid viral clearance in macrophages, while abolishing membrane ACE2-mediated
298 infection in epithelial cells. Together, these findings reveal a dual-function mechanism for
299 sACE2-Fc decoys in redirecting SARS-CoV-2 to phagocytic clearance and rapid immune
300 engagement, supporting their potential as intranasal prophylactics against respiratory viruses.

301 Previously engineered sACE2-Fc [7,11] have achieved high neutralization potency against
302 SARS-CoV-2 by incorporating up to five mutations. However, the extensive mutagenesis
303 raises concerns about structural instability [11], reduced production efficiency [4], and
304 potential immunogenicity [43]. In this study, we adopted a minimalistic approach by
305 introducing only two targeted mutations in sACE2-Fc. The optimized B5-D3 retains a
306 conformation closely resembling native ACE2 and exhibits robust viral neutralization and
307 enzymatic inactivation. These results underscore the feasibility of achieving optimal antiviral
308 potency while preserving protein stability and safety through limited mutagenesis.

309 A major challenge in controlling SARS-CoV-2 and other respiratory virus infections is that
310 systematically infused monoclonal antibodies and vaccine-induced immunity primarily target
311 viruses in the circulation, which may only represent a minor fraction of viral burden during
312 early infection. This limits their ability to respond to initial viral infection in respiratory
313 epithelium to prevent massive propagation. Our study and others' work [14] have consistently
314 shown that systemic administration of sACE2-Fc decoy or monoclonal antibodies, either
315 before or after the virus inoculation, exhibited limited efficacy against virus replication and
316 pathogenesis (Fig. 2b, blue and green lines). In contrast, prophylaxis with IN B5-D3 resulted in
317 complete protection, with 100% survival and no detectable weight loss in the −6 h group (Fig.
318 2b, g, red lines). Notably, this protection was observed in both young and aged mice, which
319 otherwise exhibited 60% and 100% mortality, respectively, following infection (Fig. 2c, h,
320 black lines). These findings underscore the importance of rapid antiviral action at the site of
321 viral entry, which is particularly crucial to protect against respiratory viruses.

322 IN prophylaxis with monoclonal antibodies or other sACE2Fc mutants have been shown to be
323 effective against SAS-CoV-2 [14,18,21], and studies have found that sACE2-Fc protects
324 against virus through the Fc-effector functions [7]. However, the precise mechanism has not
325 been depicted, which prevents the further development of these approaches for translation.
326 Here, our study provided evidence for a deeper mechanistic insight, showing that IN sACE2-Fc
327 decoys rapidly engage host immunity in the respiratory tract. Consistently with others' work
328 [7], IN delivery of a Fc-null variant (B5-D3-LALA) resulted in suboptimal protection and
329 higher viral infection compared to B5-D3. Notably, despite the minimal infection observed,
330 B5-D3-treated mice showed robust early immune activation, including induction of antigen
331 presentation and T cell activation within 24 h post-infection (Fig 4). These support that B5-D3
332 not only neutralizes virus but also primes innate and adaptive immune responses, counteracting
333 early-stage viral immune evasion.

334 Furthermore, our bio-distribution data showed that IN-delivered B5-D3 preferentially
335 accumulates in the respiratory tract (Fig. 5a–d). Flow cytometry and confocal imaging
336 confirmed strong binding and uptake of B5-D3 by airway phagocytes, primarily alveolar
337 macrophages and monocyte-derived macrophages (Fig. 5e-l). Notably, phagocytosis assays
338 demonstrated that B5-D3–virus complexes were trafficked to lysosomes for degradation in
339 macrophages. These findings support a mechanism in which B5-D3 redirects viral particles
340 away from membrane ACE2-dependent epithelial entry and toward phagocytic clearance (Fig.
341 7). Importantly, this ADCP-like process likely also facilitates early activation of pattern
342 recognition receptors (PRRs) and initiates downstream antiviral signaling cascades before the
343 virus reaches epithelial targets (Fig. 7b). Hence, the IN prophylaxis offers a unique advantage
344 by enabling localized immune priming and efficient viral clearance at the frontline of infection.

345 In conclusion, we present a rationally designed sACE2-Fc decoy with minimal mutagenesis
346 (B5-D3) and provide compelling evidence and insights into the immune mechanism supporting

its potent prophylactic efficacy. Intranasal prophylactic administration of B5-D3 not only neutralizes SARS-CoV-2 but also redirects the virus toward phagocytic clearance, enabling early immune engagement and complete protection. These findings provide a mechanistic basis for decoy-based antiviral strategies and offer a promising approach to combat current and future airborne viral threats. Further studies may aim to develop approaches to enhance the rapid local immune engagement to restrict early viral propagation. Additionally, regimen refinements are needed to enhance stability and functionality of decoy-based treatments before their clinical translation and extension to a broader range of respiratory pathogens.

MATERIALS AND METHODS

Plasmid construction

The coding sequence of human ACE2 was cloned into the pGEM-T easy vector (Promega) and underwent site-directed mutagenesis [4,11,23,33]. The sACE2 and human IgG1 hinge-Fc regions (amino acid [aa] 216-447) were assembled via overlapping PCR. These constructs, along with 6xHis-tagged versions, were inserted into the HDM-SARS2-Spike-delta21 vector (Addgene #155130) to generate HDM-CMV-sACE2(-Fc)-his plasmids. L234A/L235A (LALA) in hIgG1 were introduced to generate HDM-CMV-sACE2-Fc-LALA-his plasmids. SARS-CoV-2 spike variants with or without an HA tag fused to the C-terminal were synthesized and inserted into the HDM vector [38].

Protein structure visualization

The crystal structure of SARS-CoV-2 spike receptor-binding domain bound with ACE2 (6M0J) was downloaded from the Protein Data Bank (PDB, https://www.rcsb.org/structure/6m0j) [22]. Color-labeling of individual amino acids was performed on the PDB website. For structural overlapping analysis of wild type (WT) sACE2

371 and B5-D3 (aa 18-740), protein structures were predicted using online AlphaFold 3 server
372 (https://alphafoldserver.com/) [1]. PyMOL was utilized for root mean square deviation
373 (RMSD) calculations and structural visualization.

374 **Cell culture**

375 293T, Vero E6, Calu-3, and THP-1 cells were obtained from the American Type Culture
376 Collection and incubated at 37 °C with 5% CO_2. Specifically, 293T, Vero E6, and Calu-3 cells
377 were maintained in Dulbecco's Modified Eagle Medium (DMEM, Gibco) supplemented with
378 10% fetal bovine serum (FBS, Gibco) and 1% Penicillin-Streptomycin (PS, Gibco). THP-1
379 cells were cultured in Roswell Park Memorial Institute 1640 medium (RPMI, Gibco) with
380 similar supplements. THP-1 cells were differentiated into M0 macrophages using 50 nM
381 phorbol 12-myristate 13-acetate (PMA) for 48 h, followed by a 24 h rest. For M1 macrophage
382 differentiation, post-PMA treatment cells were stimulated with 10 ng/mL lipopolysaccharide
383 and 20 ng/mL interferon (IFN)-γ for 24 h. Expi293 cells (Gibco) were cultured following the
384 manufacturer's instructions.

385 **Immunofluorescence staining of hACE2-293T and hACE2-Calu-3**

386 Cells were fixed, permeabilized, and blocked with 10% Normal Goat Serum (Invitrogen).
387 ACE2 was stained with a primary antibody (Abcam #ab15348) followed by an Alexa Fluor
388 594-conjugated secondary antibody (Invitrogen #A-21442). Cells were counterstained with
389 Hoechst 33342 (Thermo Scientific) and examined under Nikon Ti2-E Inverted Fluorescence
390 Microscope.

391 **Lentivirus packaging and transduction**

392 293T cells were seeded at 80% confluence and transfected with psPAX2 (Addgene #12260),
393 pMD2.G (Addgene #12259), and transfer plasmid pWPI-IRES-Puro-Ak-ACE2-TMPRSS2
394 (Addgene #154987) using polyethylenimine (PEI). Lentivirus-containing medium was

395 harvested 72 h post-transfection, filtered through a 0.45 μM filter, concentrated, and stored at -
396 80°C. For transduction, 293T or Calu-3 cells were exposed to the concentrated lentivirus with 8
397 μg/mL polybrene for 24 h to obtain human ACE2-overexpressing cell lines (hACE2-293T and
398 hACE2-Calu-3 respectively).

399 **Pseudovirus packaging, titration, and infection**

400 Pseudoviruses were packaged in 293T cells using pCDH-EF1a-eFFly-eGFP (Addgene
401 #104834) and spike-encoding plasmids, following a similar protocol to that of lentivirus. Post-
402 packaging, pseudoviral particles were titrated using the Lenti-X qRT-PCR Titration Kit (Takara
403 #631235) and used to infect target cells in the presence of 8 μg/mL polybrene. Infectivity was
404 assessed via a luciferase assay (Promega #E1501).

405 **Protein production and purification**

406 293T and Expi293 cells were transfected with HDM-CMV-sACE2(-Fc)(-LALA)-his plasmids
407 using PEI and ExpiFectamine 293 Transfection Kit (Gibco) respectively. Culture supernatants
408 were collected after 72 h and 5 days post-transfection respectively. The 293T supernatant was
409 assessed for ACE2 and IgG1 levels using enzyme-linked immunosorbent assay (ELISA) kits
410 (Abcam #ab235649; Invitrogen #BMS2092), and ACE2 activity was measured with a
411 fluorometric assay (Abcam # ab273297). The Expi293 supernatant underwent Ni-NTA Agarose
412 purification, followed by elution and buffer exchange to phosphate-buffered saline (PBS, pH
413 7.4). Protein concentration and integrity were verified using the Bradford method, ELISA, and
414 sodium dodecyl sulfate-polyacrylamide gel electrophoresis (SDS-PAGE).

415 ***In vitro* pseudovirus neutralization assay**

416 Conditioned media containing sACE2, sACE2-Fc or sACE2-Fc-LALA proteins were diluted
417 serially, mixed with pseudovirus (4×10^9 copies), and incubated at room temperature for 30
418 minutes [9]. The mixture was added to hACE2-293T cells in 96-well plates with duplicates

419 with 8 μg/mL polybrene. Transduction efficiency was assessed 48 h later via green fluorescent
420 protein (GFP) imaging and/or luciferase assays.

421 **Reporter-based *in vitro* ADCC and ADCP assays**

422 The *in vitro* antibody-dependent cell-mediated cytotoxicity (ADCC) and antibody-dependent
423 cellular phagocytosis (ADCP) activities of B5-D3(-LALA) were measured using Jurkat-Lucia
424 NFAT-CD16 and Jurkat-Lucia NFAT-CD32 cells (InvivoGen) respectively according to the
425 manufacturer's instructions. 293T cells transfected with pBOB-CAG-SARS-CoV-2-Spike-HA
426 (Addgene #141347) acted as target cells. Target cells were co-incubated with reporter cells and
427 serially diluted B5-D3(-LALA) at 37°C for 1 h. Luciferase expression indicating CD16 and
428 CD32 signaling was measured using QUANTI-Luc (InvivoGen).

429 **ADCP of pseudovirus and confocal imaging**

430 SARS-CoV-2 pseudovirus (8×10^8 copies) was incubated with sACE2-Fc and target cells in μ-
431 Slide 18 Well chamber slides (ibidi). After 6 h, cells were fixed, blocked, and immunostained
432 for human IgG-Fc (Abcam #ab98596), human immunodeficiency virus (HIV)-1 p24
433 (Invitrogen #PA5-81773), and lysosomal associated membrane protein 1 (LAMP1) (Abcam
434 #ab25630). Secondary antibodies were applied (Invitrogen #A-21200 and #A-31573), and
435 nuclei were stained with Hoechst. Confocal microscopy (Leica TCS SP8) and ImageJ software
436 with the JACoP plugin were used to assess p24 fluorescence and its colocalization with
437 LAMP1.

438 **Western blot for spike cleavage detection**

439 SARS-CoV-2 spike-HA tagged pseudovirus (4×10^9 copies) was incubated with M0/M1
440 macrophages or hACE2-293T cells for 6 h, with or without sACE2-Fc proteins. After
441 incubation, cell lysates were processed through SDS-PAGE and transferred to polyvinylidene

442 difluoride membranes. The membranes were blocked, incubated overnight with anti-HA
443 (Merck Millipore #05-904) and anti-β-actin (Santa Cruz #sc-47778) primary antibodies, then
444 with horseradish peroxidase (HRP)-conjugated secondary antibodies (Cell Signaling
445 Technology #7076). Signals were detected using the Amersham ECL select kit on a Bio-Rad
446 ChemiDoc MP system.

447 **Quantitative PCR**

448 Quantitative PCR (qPCR) was used to analyze lung RNA from mice. RNA was extracted from
449 lung tissues using TRIzol (Invitrogen), reverse-transcribed (Applied Biosystems #4368813),
450 and amplified using the TB Green Premix Ex Taq II kit (Takara), normalized to mouse *Gapdh*
451 using the 2^-ΔCt method. qPCRs were run in duplicates on 384-well plates, with specific
452 primers listed in Supplementary Table 1.

453 **SARS-CoV-2 virus**

454 Experiments with live SARS-CoV-2 were performed at the BSL-3 core facility (LKS Faculty
455 of Medicine, HKU). The BetaCoV/Hong Kong/VM20001061/2020 virus, here regarded as the
456 wild type strain of SARS-CoV-2 (Wuhan-Hu-1), was isolated from the nasopharyngeal aspirate
457 and throat swab of a confirmed patient with COVID-19 in Hong Kong (GISAID identifier
458 EPI_ISL_412028). The SARS-CoV-2 variants were isolated from clinical specimens in Hong
459 Kong. Stock viruses were prepared with Vero E6 cells cultured in infection medium (DMEM
460 supplemented with 2% FBS and 1% PS).

461 **Median tissue culture infectious dose ($TCID_{50}$) assay**

462 Vero E6 cells pre-seeded in 96-well plates were infected with serially diluted virus stocks or
463 mouse lung homogenates in infection medium. After 72 h incubation, cytopathic effects (CPEs)
464 were observed under a microscope to calculate titers using the Reed–Muench method.

465 **Plaque-reduction neutralization test (PRNT) assay**

466 Proteins were serially diluted and pre-incubated with SARS-CoV-2 variants, followed by
467 addition to Vero E6 cells seeded in 6-well plates. After incubation, cells were overlaid with
468 agarose, fixed with formalin, and stained with crystal violet. Plaque counts were used to
469 calculate percentage neutralization and half maximal inhibitory concentration (IC_{50}) values.

470 **Animal experiments**

471 Experiments on protein-only administration in mice were carried out in the Animal Holding
472 Core of the School of Biomedical Sciences, CUHK. Experiments involving SARS-CoV-2
473 infection in K18-hACE2 mice were conducted within the confines of the Biosafety Level 3
474 (BSL-3) core facility located at the Li Ka Shing Faculty of Medicine, HKU. Experiments were
475 conducted according to ethical practices to minimize animal distress.

476 **SARS-CoV-2 infection in mice**

477 Female K18-hACE2 mice, aged 10-12 months or 2-3 months, were intranasally inoculated
478 with 1×10^4 plaque-forming unit (PFU) of SARS-CoV-2 Wuhan-Hu-1. Treatment with B5-D3
479 protein was administered intranasally at 2.5 mg/kg or intravenously at 15 mg/kg, at various
480 time points relative to the viral challenge (6 h before, 24 h before, or 24 h after). Vehicle
481 control groups received PBS 6 h before viral challenge. Survival and weight were monitored
482 daily for 14 days. For the older mice, lung samples were collected from one mouse from each
483 group at 4 days post-infection (dpi) for analysis; younger mice had plasma collected for
484 neutralizing antibody analysis at 14 dpi. Another batch of young mice also received B5-D3(-
485 LALA) protein pre-inoculation, with lungs analyzed post-inoculation for RNA, viral load, and
486 histopathology. A control group of non-infected mice was used to assess baseline effects of B5-
487 D3 on lung tissue.

488 **Neutralization assay for antibody titration**

489 Vero E6 cells were pre-seeded on 96-well plates 24 h before infection. On the day of infection,

the growth medium of the cells was changed to infection medium. The plasma samples were serially 2-fold diluted with infection medium from a starting dilution of 1:10. The plasma was then pre-incubated with 100 $TCID_{50}$ of SARS-CoV-2 for 1 h at room temperature before being inoculated to the seeded Vero E6 cells in quadruplicates. At 72 h after inoculation, CPEs of the cells were observed with optical microscopy. Neutralizing antibody titers against SARS-CoV-2 were expressed as the reciprocal of the highest dilution of plasma showing no CPEs in all 4 wells. Uninfected cell monolayers were used as toxicity control.

Histology

Mouse tissues were fixed in 10% formalin, embedded in paraffin, and sectioned at 5 μm. Sections of different organs were deparaffinized and underwent hematoxylin and eosin (H&E) staining. For immunohistochemistry (IHC) staining, lung sections underwent antigen retrieval, endogenous peroxidase blocking, and were incubated with primary antibodies against the SARS-CoV/SARS-CoV-2 nucleocapsid protein (Sino Biological #40143-T62) overnight. After washing, sections were stained with the anti-rabbit VECTASTAIN Elite ABC-HRP Kit (Vector Laboratories), developed with 3,3′-Diaminobenzidine (Sigma #D4293), and counterstained with Mayer's hematoxylin.

RNA-Seq and data analysis

Total RNA was extracted from lung tissues using TRIzol and processed into transcriptome libraries with the TruSeq RNA Library Prep Kit (illumina). Sequencing was performed on the NovaSeq 6000 sequencer (illumina) using a 150-base pair paired-end configuration. Sequencing data were processed with fastp for quality control [6], then aligned to both the mouse (Ensembl GRCm39) and SARS-CoV-2 (NCBI NC_045512v2) genomes using STAR [29]. Pearson correlation and groupwise comparisons were conducted in R: gene expression was quantified and analyzed for differential expression using DESeq2 [27]; up/downregulated

gene enrichment and Gene Set Enrichment Analysis (GSEA) [39] was performed using the clusterProfiler package [48].

Tracking B5-D3 bio-distribution in mice

B5-D3 were conjugated with Alexa Fluor 750 dye (B5-D3-AF750) as described [21]. In brief, 2 mg/mL solution of B5-D3 protein in 0.1M $NaHCO_3$ was reacted with Alexa Fluor 750 succinimidyl ester (Thermo Fisher Scientific) at room temperature for 1 h. Unreacted dye was removed by dialysis in PBS. All procedures were performed under dimmed light. Female K18-hACE2 mice, aged 2-3 month, were administered intranasally with B5-D3-AF750 (2.5 mg/kg). The mice were imaged at predetermined time points after administration (fluorescence ex = 745 nm, em = 800 nm, auto-exposure setting) using an IVIS Spectrum CT Imager (Perkin Elmer). At the time of euthanasia, 50 μl of urine and blood, the brain, nasal cavity, trachea, lung, heart, liver, spleen, kidney, and urinary bladder samples were excised and imaged. Regions of interest (ROIs) were drawn, and average radiance ($p/s/cm^2/sr$) was measured. All images were processed using Living Image software (Perkin Elmer) and the same fluorescence threshold was applied for group comparison.

Flow cytometry analysis and confocal microscopic imaging of BALF cells

Mice were sacrificed via anesthetics overdose. Bronchoalveolar lavage was performed by intratracheally rinsing the lungs with 1 mL of ice-cold Hanks' Balanced Salt Solution (HBSS, Gibco) containing 100 μM ethylenediaminetetraacetic acid for four repeats. Bronchoalveolar lavage fluid (BALF) was then centrifuged and treated with ammonium-chloride-potassium red blood cell lysing buffer. Cell pellets were washed with PBS and stained with the Fixable Viability Stain 440UV dye (BD #566332). Next, the cells were blocked with CD16/CD32 monoclonal antibody (Invitrogen #14-0161-85) and stained with antibodies targeting the following molecules: CD45 (BD #568336), Siglec-F (BD #564514), CD11b (BD #612800), CD11c (BD #751265), Ly6G (BD #563005), I-A/I-E major histocompatibility complex class II

(MHC-II) (BD #750171), F4/80 (BD #570288), Ly6C (BD #755198), and CD3 (BD #555275). Stained BALF cells were analyzed using the BD FACSymphony A5.2 SORP Flow Cell Analyzer, and the results were analyzed using FlowJo v10.10.

For microscopic inspections, BALF cells were seeded in poly-d-lysine-coated chamber slides and stained with antibodies targeting Siglec-F (BD #564514) and human IgG-Fc (Abcam #ab98596). Secondary antibody (Invitrogen #A-11006) was applied to amplify Siglec-F signal. Stained BALF cells were then counterstained with Hoechst and examined by confocal microscopy (Leica TCS SP8).

Statistical Analysis

Assays including *in vitro* neutralization, PRNT, ADCC, and ADCP were conducted in technical duplicates. Results were analyzed in GraphPad Prism version 9 using nonlinear regression to calculate IC_{50} or half maximal effective concentration (EC_{50}) values. Transcriptomic analyses were performed using R, with details provided in figure captions. All other statistical analyses utilized GraphPad Prism version 9 with a significance threshold set at p value (p) < 0.05.

SUPPLEMENTARY INFORMATION

This PDF file includes:

Fig. S1 to S15; Table S1.

DECLARATIONS

Ethics approval and consent to participate

All animal procedures were ethically approved by The Chinese University of Hong Kong (CUHK)'s Animal Experimentation Ethics Committee (approval number: 20-226-MIS) and

562 The University of Hong Kong (HKU)'s Committee on the Use of Live Animals in Teaching
563 and Research (approval number: 5511-20).

564 **Availability of data and materials**

565 All data associated with this study are available in the main text or the supplementary
566 materials. The RNA-seq data generated in this study have been deposited in the NCBI
567 Sequence Read Archive database under accession code PRJNA1054508. Constructs of diverse
568 sACE2-Fc mutants and SARS-CoV-2 spikes are available upon request after completion and
569 approval of a material transfer agreement by contacting fengbo@cuhk.edu.hk.

570 **Competing interests**

571 The authors declare that they have no competing interests.

572 **Funding**

573 This study was supported by Research Grants Council of Hong Kong grants 14115520,
574 14106024 (B.F.), C7145-20GF (L.L.P.), and in part by the Health@InnoHK Program launched
575 by Innovation Technology Commission of the Hong Kong SAR, China. Jingyi W., J.L, B.L.,
576 and J.Q. received postgraduate studentships from the Chinese University of Hong Kong.

577 **Authors' contributions**

578 Jingyi W. and J.L. constructed the sACE2-Fc mutants and performed characterization analysis;
579 A.W.C. performed the PRNTs and data analysis; Jingyi W., A.W.C., and J.L. performed the
580 mouse infection experiments and data analysis; B.L., J.Q. and J.R. produced recombinant
581 sACE2-Fc proteins; Jingyi W. and Junkang W. performed RNA-Seq analysis; Jingyi W. and
582 J.Q. performed protein labeling, *in vivo* tracing of labeled protein, and flow cytometry analysis
583 of BALF cells; J.L. performed THP-1 and Calu-3 experiments and confocal microscopic
584 analysis. Junkang W. and J.L. performed protein structure prediction and visualization. Jingyi
585 W., J.L., L.L.P. and B.F. conceived the project, designed experiments, and wrote the

586 manuscript. Y.X., T.B., L.L.P. and B.F. revised the manuscript. All authors read and approved
587 the final manuscript.

588 **Acknowledgements**

589 We thank the Chinese University of Hong Kong (CUHK) and the University of Hong Kong
590 (HKU) research platforms for assistance in animal experimentation (the Laboratory Animal
591 Service Center at CUHK and the Centre for Comparative Medicine Research at HKU) and
592 histological analysis (Department of Pathology, HKU and Core Laboratory in the School of
593 Biomedical Sciences, CUHK).

594

595 **REFERENCES**

596 1. Abramson J., Adler J., Dunger J., Evans R., Green T., Pritzel A., Ronneberger O., Willmore L., Ballard
597 A.J., Bambrick J., Bodenstein S.W., Evans D.A., Hung C.-C., O'Neill M., Reiman D., Tunyasuvunakool
598 K., Wu Z., Žemgulytė A., Arvaniti E., Beattie C., Bertolli O., Bridgland A., Cherepanov A., Congreve
599 M., Cowen-Rivers A.I., Cowie A., Figurnov M., Fuchs F.B., Gladman H., Jain R., Khan Y.A., Low
600 C.M.R., Perlin K., Potapenko A., Savy P., Singh S., Stecula A., Thillaisundaram A., Tong C., Yakneen S.,
601 Zhong E.D., Zielinski M., Žídek A., Bapst V., Kohli P., Jaderberg M., Hassabis D. and Jumper J.M.
602 Accurate structure prediction of biomolecular interactions with AlphaFold 3. Nature 630(8016):493-500,
603 2024.
604 2. Amin R., Pal P., Dhama K. and Emran T.B. Recent update on XBB.1.5 emerging novel mutation of
605 COVID-19. International Journal of Surgery 109(4):1048-1049, 2023.
606 3. Cao Y., Wang J., Jian F., Xiao T., Song W., Yisimayi A., Huang W., Li Q., Wang P., An R., Wang J., Wang
607 Y., Niu X., Yang S., Liang H., Sun H., Li T., Yu Y., Cui Q., Liu S., Yang X., Du S., Zhang Z., Hao X.,
608 Shao F., Jin R., Wang X., Xiao J., Wang Y. and Xie X.S. Omicron escapes the majority of existing SARS-
609 CoV-2 neutralizing antibodies. Nature 602(7898):657-663, 2022.
610 4. Chan K.K., Dorosky D., Sharma P., Abbasi S.A., Dye J.M., Kranz D.M., Herbert A.S. and Procko E.
611 Engineering human ACE2 to optimize binding to the spike protein of SARS coronavirus 2. Science
612 369(6508):1261-1265, 2020.
613 5. Chanput W., Mes J.J. and Wichers H.J. THP-1 cell line: An in vitro cell model for immune modulation
614 approach. International Immunopharmacology 23(1):37-45, 2014.
615 6. Chen S., Zhou Y., Chen Y. and Gu J. fastp: an ultra-fast all-in-one FASTQ preprocessor. Bioinformatics
616 34(17):i884-i890, 2018.
617 7. Chen Y., Sun L., Ullah I., Beaudoin-Bussières G., Anand S.P., Hederman A.P., Tolbert W.D., Sherburn R.,
618 Nguyen D.N., Marchitto L., Ding S., Wu D., Luo Y., Gottumukkala S., Moran S., Kumar P., Piszczek G.,
619 Mothes W., Ackerman M.E., Finzi A., Uchil P.D., Gonzalez F.J. and Pazgier M. Engineered ACE2-Fc
620 counters murine lethal SARS-CoV-2 infection through direct neutralization and Fc-effector activities.
621 Science Advances 8(28):eabn4188, 2022.
622 8. Colomer-Molera M., Sastre D., Sole Codina L., Vallejo-Gracia A., Navarro Perez M., Capera-Aragones

J., Estadella I., Cassinelli S., Panyi G., Hajdu P.B., Tamkun M.M. and Felipe A. Kv1.3-dependent immune system activation is regulated by KCNE4. Biophysical Journal 122(3):14a, 2023.

9. Crawford K.H.D., Eguia R., Dingens A.S., Loes A.N., Malone K.D., Wolf C.R., Chu H.Y., Tortorici M.A., Veesler D., Murphy M., Pettie D., King N.P., Balazs A.B. and Bloom J.D. Protocol and Reagents for Pseudotyping Lentiviral Particles with SARS-CoV-2 Spike Protein for Neutralization Assays. Viruses 12(5):513, 2020.

10. Garcia-Beltran W.F., Lam E.C., St. Denis K., Nitido A.D., Garcia Z.H., Hauser B.M., Feldman J., Pavlovic M.N., Gregory D.J., Poznansky M.C., Sigal A., Schmidt A.G., Iafrate A.J., Naranbhai V. and Balazs A.B. Multiple SARS-CoV-2 variants escape neutralization by vaccine-induced humoral immunity. Cell 184(9):2372-2383.e2379, 2021.

11. Glasgow A., Glasgow J., Limonta D., Solomon P., Lui I., Zhang Y., Nix M.A., Rettko N.J., Zha S., Yamin R., Kao K., Rosenberg O.S., Ravetch J.V., Wiita A.P., Leung K.K., Lim S.A., Zhou X.X., Hobman T.C., Kortemme T. and Wells J.A. Engineered ACE2 receptor traps potently neutralize SARS-CoV-2. Proceedings of the National Academy of Sciences 117(45):28046-28055, 2020.

12. Guy J.L., Jackson R.M., Jensen H.A., Hooper N.M. and Turner A.J. Identification of critical active-site residues in angiotensin-converting enzyme-2 (ACE2) by site-directed mutagenesis. The FEBS Journal 272(14):3512-3520, 2005.

13. Halfmann P.J., Kuroda M., Armbrust T., Theiler J., Balaram A., Moreno G.K., Accola M.A., Iwatsuki-Horimoto K., Valdez R., Stoneman E., Braun K., Yamayoshi S., Somsen E., Baczenas J.J., Mitamura K., Hagihara M., Adachi E., Koga M., McLaughlin M., Rehrauer W., Imai M., Yamamoto S., Tsutsumi T., Saito M., Friedrich T.C., O'Connor S.L., O'Connor D.H., Gordon A., Korber B. and Kawaoka Y. Characterization of the SARS-CoV-2 B.1.621 (Mu) variant. Science Translational Medicine 14(657):eabm4908, 2022.

14. Hassler L., Wysocki J., Ahrendsen J.T., Ye M., Gelarden I., Nicolaescu V., Tomatsidou A., Gula H., Cianfarini C., Forster P., Khurram N., Singer B.D., Randall G., Missiakas D., Henkin J. and Batlle D. Intranasal soluble ACE2 improves survival and prevents brain SARS-CoV-2 infection. Life Science Alliance 6(7):e202301969, 2023.

15. Hoffmann M., Kleine-Weber H., Schroeder S., Krüger N., Herrler T., Erichsen S., Schiergens T.S., Herrler G., Wu N.-H., Nitsche A., Müller M.A., Drosten C. and Pöhlmann S. SARS-CoV-2 Cell Entry Depends on ACE2 and TMPRSS2 and Is Blocked by a Clinically Proven Protease Inhibitor. Cell 181(2):271-280.e278, 2020.

16. Katagiri K., Hattori M., Minato N. and Kinashi T. Rap1 Functions as a Key Regulator of T-Cell and Antigen-Presenting Cell Interactions and Modulates T-Cell Responses. Molecular and Cellular Biology 22(4):1001-1015, 2002.

17. Kimura I., Kosugi Y., Wu J., Zahradnik J., Yamasoba D., Butlertanaka E.P., Tanaka Y.L., Uriu K., Liu Y., Morizako N., Shirakawa K., Kazuma Y., Nomura R., Horisawa Y., Tokunaga K., Ueno T., Takaori-Kondo A., Schreiber G., Arase H., Motozono C., Saito A., Nakagawa S. and Sato K. The SARS-CoV-2 Lambda variant exhibits enhanced infectivity and immune resistance. Cell Reports 38(2):110218, 2022.

18. Kober D.L., Dyke M.C.C.V., Eitson J.L., Boys I.N., McDougal M.B., Rosenbaum D.M. and Schoggins J.W. Development of a mutant aerosolized ACE2 that neutralizes SARS-CoV-2 *in vivo*. mBio 15(6):e00768-00724, 2024.

19. Korber B., Fischer W.M., Gnanakaran S., Yoon H., Theiler J., Abfalterer W., Hengartner N., Giorgi E.E., Bhattacharya T., Foley B., Hastie K.M., Parker M.D., Partridge D.G., Evans C.M., Freeman T.M., de Silva T.I., Angyal A., Brown R.L., Carrilero L., Green L.R., Groves D.C., Johnson K.J., Keeley A.J., Lindsey B.B., Parsons P.J., Raza M., Rowland-Jones S., Smith N., Tucker R.M., Wang D., Wyles M.D.,

McDanal C., Perez L.G., Tang H., Moon-Walker A., Whelan S.P., LaBranche C.C., Saphire E.O. and Montefiori D.C. Tracking Changes in SARS-CoV-2 Spike: Evidence that D614G Increases Infectivity of the COVID-19 Virus. Cell 182(4):812-827.e819, 2020.

20. Korobova Z.R., Arsentieva N.A. and Totolian A.A. Macrophage-Derived Chemokine MDC/CCL22: An Ambiguous Finding in COVID-19. International Journal of Molecular Sciences 24(17):13083, 2023.

21. Ku Z., Xie X., Hinton P.R., Liu X., Ye X., Muruato A.E., Ng D.C., Biswas S., Zou J., Liu Y., Pandya D., Menachery V.D., Rahman S., Cao Y.-A., Deng H., Xiong W., Carlin K.B., Liu J., Su H., Haanes E.J., Keyt B.A., Zhang N., Carroll S.F., Shi P.-Y. and An Z. Nasal delivery of an IgM offers broad protection from SARS-CoV-2 variants. Nature 595(7869):718-723, 2021.

22. Lan J., Ge J., Yu J., Shan S., Zhou H., Fan S., Zhang Q., Shi X., Wang Q., Zhang L. and Wang X. Structure of the SARS-CoV-2 spike receptor-binding domain bound to the ACE2 receptor. Nature 581(7807):215-220, 2020.

23. Lei C., Qian K., Li T., Zhang S., Fu W., Ding M. and Hu S. Neutralization of SARS-CoV-2 spike pseudotyped virus by recombinant ACE2-Ig. Nature Communications 11(1):2070, 2020.

24. Li L., Liao H., Meng Y., Li W., Han P., Liu K., Wang Q., Li D., Zhang Y., Wang L., Fan Z., Zhang Y., Wang Q., Zhao X., Sun Y., Huang N., Qi J. and Gao G.F. Structural basis of human ACE2 higher binding affinity to currently circulating Omicron SARS-CoV-2 sub-variants BA.2 and BA.1.1. Cell 185(16):2952-2960.e2910, 2022.

25. Liu P., Wysocki J., Souma T., Ye M., Ramirez V., Zhou B., Wilsbacher L.D., Quaggin S.E., Batlle D. and Jin J. Novel ACE2-Fc chimeric fusion provides long-lasting hypertension control and organ protection in mouse models of systemic renin angiotensin system activation. Kidney International 94(1):114-125, 2018.

26. Liu P., Xie X., Gao L. and Jin J. Designed variants of ACE2-Fc that decouple anti-SARS-CoV-2 activities from unwanted cardiovascular effects. Int J Biol Macromol 165(Pt B):1626-1633, 2020.

27. Love M.I., Huber W. and Anders S. Moderated estimation of fold change and dispersion for RNA-seq data with DESeq2. Genome Biology 15(12):550, 2014.

28. Lund J., Winter G., Jones P.T., Pound J.D., Tanaka T., Walker M.R., Artymiuk P.J., Arata Y., Burton D.R., Jefferis R. and Woof J.M. Human Fc gamma RI and Fc gamma RII interact with distinct but overlapping sites on human IgG. The Journal of Immunology 147(8):2657-2662, 1991.

29. Maulding N.D., Seiler S., Pearson A., Kreusser N. and Stuart J.M. Dual RNA-Seq analysis of SARS-CoV-2 correlates specific human transcriptional response pathways directly to viral expression. Scientific Reports 12(1):1329, 2022.

30. Mlcochova P., Kemp S.A., Dhar M.S., Papa G., Meng B., Ferreira I.A.T.M., Datir R., Collier D.A., Albecka A., Singh S., Pandey R., Brown J., Zhou J., Goonawardane N., Mishra S., Whittaker C., Mellan T., Marwal R., Datta M., Sengupta S., Ponnusamy K., Radhakrishnan V.S., Abdullahi A., Charles O., Chattopadhyay P., Devi P., Caputo D., Peacock T., Wattal C., Goel N., Satwik A., Vaishya R., Agarwal M., Chauhan H., Dikid T., Gogia H., Lall H., Verma K., Dhar M.S., Singh M.K., Soni N., Meena N., Madan P., Singh P., Sharma R., Sharma R., Kabra S., Kumar S., Kumari S., Sharma U., Chaudhary U., Sivasubbu S., Scaria V., Oberoi J.K., Raveendran R., Datta S., Das S., Maitra A., Chinnaswamy S., Biswas N.K., Parida A., Raghav S.K., Prasad P., Sarin A., Mayor S., Ramakrishnan U., Palakodeti D., Seshasayee A.S.N., Thangaraj K., Bashyam M.D., Dalal A., Bhat M., Shouche Y., Pillai A., Abraham P., Potdar V.A., Cherian S.S., Desai A.S., Pattabiraman C., Manjunatha M.V., Mani R.S., Udupi G.A., Nandicoori V., Tallapaka K.B., Sowpati D.T., Kawabata R., Morizako N., Sadamasu K., Asakura H., Nagashima M., Yoshimura K., Ito J., Kimura I., Uriu K., Kosugi Y., Suganami M., Oide A., Yokoyama M., Chiba M., Saito A., Butlertanaka E.P., Tanaka Y.L., Ikeda T., Motozono C., Nasser H., Shimizu R.,

Yuan Y., Kitazato K., Hasebe H., Nakagawa S., Wu J., Takahashi M., Fukuhara T., Shimizu K., Tsushima K., Kubo H., Shirakawa K., Kazuma Y., Nomura R., Horisawa Y., Takaori-Kondo A., Tokunaga K., Ozono S., Baker S., Dougan G., Hess C., Kingston N., Lehner P.J., Lyons P.A., Matheson N.J., Owehand W.H., Saunders C., Summers C., Thaventhiran J.E.D., Toshner M., Weekes M.P., Maxwell P., Shaw A., Bucke A., Calder J., Canna L., Domingo J., Elmer A., Fuller S., Harris J., Hewitt S., Kennet J., Jose S., Kourampa J., Meadows A., O'Brien C., Price J., Publico C., Rastall R., Ribeiro C., Rowlands J., Ruffolo V., Tordesillas H., Bullman B., Dunmore B.J., Fawke S., Gräf S., Hodgson J., Huang C., Hunter K., Jones E., Legchenko E., Matara C., Martin J., Mescia F., O'Donnell C., Pointon L., Pond N., Shih J., Sutcliffe R., Tilly T., Treacy C., Tong Z., Wood J., Wylot M., Bergamaschi L., Betancourt A., Bower G., Cossetti C., De Sa A., Epping M., Fawke S., Gleadall N., Grenfell R., Hinch A., Huhn O., Jackson S., Jarvis I., Krishna B., Lewis D., Marsden J., Nice F., Okecha G., Omarjee O., Perera M., Potts M., Richoz N., Romashova V., Yarkoni N.S., Sharma R., Stefanucci L., Stephens J., Strezlecki M., Turner L., De Bie E.M.D.D., Bunclark K., Josipovic M., Mackay M., Rossi S., Selvan M., Spencer S., Yong C., Allison J., Butcher H., Caputo D., Clapham-Riley D., Dewhurst E., Furlong A., Graves B., Gray J., Ivers T., Kasanicki M., Le Gresley E., Linger R., Meloy S., Muldoon F., Ovington N., Papadia S., Phelan I., Stark H., Stirrups K.E., Townsend P., Walker N., Webster J., Scholtes I., Hein S., King R., Mavousian A., Lee J.H., Bassi J., Silacci-Fegni C., Saliba C., Pinto D., Irie T., Yoshida I., Hamilton W.L., Sato K., Bhatt S., Flaxman S., James L.C., Corti D., Piccoli L., Barclay W.S., Rakshit P., Agrawal A., Gupta R.K., The Indian S.-C.-G.C., The Genotype to Phenotype Japan C. and The C.-N.B.C.-C. SARS-CoV-2 B.1.617.2 Delta variant replication and immune evasion. Nature 599(7883):114-119, 2021.

31. Monteil V., Kwon H., Prado P., Hagelkrüys A., Wimmer R.A., Stahl M., Leopoldi A., Garreta E., Hurtado del Pozo C., Prosper F., Romero J.P., Wirnsberger G., Zhang H., Slutsky A.S., Conder R., Montserrat N., Mirazimi A. and Penninger J.M. Inhibition of SARS-CoV-2 Infections in Engineered Human Tissues Using Clinical-Grade Soluble Human ACE2. Cell 181(4):905-913.e907, 2020.

32. Ozono S., Zhang Y., Ode H., Sano K., Tan T.S., Imai K., Miyoshi K., Kishigami S., Ueno T., Iwatani Y., Suzuki T. and Tokunaga K. SARS-CoV-2 D614G spike mutation increases entry efficiency with enhanced ACE2-binding affinity. Nature Communications 12(1):848, 2021.

33. Payandeh Z., Rahbar M.R., Jahangiri A., Hashemi Z.S., Zakeri A., Jafarisani M., Rasaee M.J. and Khalili S. Design of an engineered ACE2 as a novel therapeutics against COVID-19. Journal of Theoretical Biology 505:110425, 2020.

34. Ramanathan M., Ferguson I.D., Miao W. and Khavari P.A. SARS-CoV-2 B.1.1.7 and B.1.351 spike variants bind human ACE2 with increased affinity. The Lancet Infectious Diseases 21(8):1070, 2021.

35. Rapp M., Wintergerst M.W.M., Kunz W.G., Vetter V.K., Knott M.M.L., Lisowski D., Haubner S., Moder S., Thaler R., Eiber S., Meyer B., Röhrle N., Piseddu I., Grassmann S., Layritz P., Kühnemuth B., Stutte S., Bourquin C., von Andrian U.H., Endres S. and Anz D. CCL22 controls immunity by promoting regulatory T cell communication with dendritic cells in lymph nodes. Journal of Experimental Medicine 216(5):1170-1181, 2019.

36. Santos R.A.S., Sampaio W.O., Alzamora A.C., Motta-Santos D., Alenina N., Bader M. and Campagnole-Santos M.J. The ACE2/Angiotensin-(1-7)/MAS Axis of the Renin-Angiotensin System: Focus on Angiotensin-(1-7). Physiol Rev 98(1):505-553, 2018.

37. Shan Q., Li X., Chen X., Zeng Z., Zhu S., Gai K., Peng W. and Xue H.-H. Tcf1 and Lef1 provide constant supervision to mature CD8+ T cell identity and function by organizing genomic architecture. Nature Communications 12(1):5863, 2021.

38. Shu Y. and McCauley J. GISAID: Global initiative on sharing all influenza data – from vision to reality. Eurosurveillance 22(13):30494, 2017.

39. Subramanian A., Tamayo P., Mootha V.K., Mukherjee S., Ebert B.L., Gillette M.A., Paulovich A., Pomeroy S.L., Golub T.R., Lander E.S. and Mesirov J.P. Gene set enrichment analysis: A knowledge-based approach for interpreting genome-wide expression profiles. Proceedings of the National Academy of Sciences 102(43):15545-15550, 2005.

40. Suryamohan K., Diwanji D., Stawiski E.W., Gupta R., Miersch S., Liu J., Chen C., Jiang Y.-P., Fellouse F.A., Sathirapongsasuti J.F., Albers P.K., Deepak T., Saberianfar R., Ratan A., Washburn G., Mis M., Santhosh D., Somasekar S., Hiranjith G.H., Vargas D., Mohan S., Phalke S., Kuriakose B., Antony A., Ustav Jr M., Schuster S.C., Sidhu S., Junutula J.R., Jura N. and Seshagiri S. Human ACE2 receptor polymorphisms and altered susceptibility to SARS-CoV-2. Communications Biology 4(1):475, 2021.

41. Takeda K. and Akira S. Toll-like receptors in innate immunity. International Immunology 17(1):1-14, 2005.

42. Tedesco S., De Majo F., Kim J., Trenti A., Trevisi L., Fadini G.P., Bolego C., Zandstra P.W., Cignarella A. and Vitiello L. Convenience versus Biological Significance: Are PMA-Differentiated THP-1 Cells a Reliable Substitute for Blood-Derived Macrophages When Studying in Vitro Polarization? Frontiers in Pharmacology 9, 2018.

43. Urano E., Itoh Y., Suzuki T., Sasaki T., Kishikawa J.-i., Akamatsu K., Higuchi Y., Sakai Y., Okamura T., Mitoma S., Sugihara F., Takada A., Kimura M., Nakao S., Hirose M., Sasaki T., Koketsu R., Tsuji S., Yanagida S., Shioda T., Hara E., Matoba S., Matsuura Y., Kanda Y., Arase H., Okada M., Takagi J., Kato T., Hoshino A., Yasutomi Y., Saito A. and Okamoto T. An inhaled ACE2 decoy confers protection against SARS-CoV-2 infection in preclinical models. Science Translational Medicine 15(711):eadi2623, 2023.

44. Wang Q., Iketani S., Li Z., Liu L., Guo Y., Huang Y., Bowen A.D., Liu M., Wang M., Yu J., Valdez R., Lauring A.S., Sheng Z., Wang H.H., Gordon A., Liu L. and Ho D.D. Alarming antibody evasion properties of rising SARS-CoV-2 BQ and XBB subvariants. Cell 186(2):279-286.e278, 2023.

45. Wang S., Niu P., Su Q., He X., Tang J., Wang J., Feng Y., Chen C., Zhao X., Chen Z., Wang W., Yin Z., Wu Y., Wu C., Li L., Cui A., Zhang Y., Long C., Yang X., Zhang Z., Bo H., Xu W. and Sars-Co V.G.W.G. Genomic Surveillance for SARS-CoV-2 - China, September 26, 2022 to January 29, 2023. China CDC weekly 5(7):143-151, 2023.

46. Weinreich D.M., Sivapalasingam S., Norton T., Ali S., Gao H., Bhore R., Xiao J., Hooper A.T., Hamilton J.D., Musser B.J., Rofail D., Hussein M., Im J., Atmodjo D.Y., Perry C., Pan C., Mahmood A., Hosain R., Davis J.D., Turner K.C., Baum A., Kyratsous C.A., Kim Y., Cook A., Kampman W., Roque-Guerrero L., Acloque G., Aazami H., Cannon K., Simón-Campos J.A., Bocchini J.A., Kowal B., DiCioccio A.T., Soo Y., Geba G.P., Stahl N., Lipsich L., Braunstein N., Herman G. and Yancopoulos G.D. REGEN-COV Antibody Combination and Outcomes in Outpatients with Covid-19. New England Journal of Medicine 385(23):e81, 2021.

47. Winkler E.S., Bailey A.L., Kafai N.M., Nair S., McCune B.T., Yu J., Fox J.M., Chen R.E., Earnest J.T., Keeler S.P., Ritter J.H., Kang L.-I., Dort S., Robichaud A., Head R., Holtzman M.J. and Diamond M.S. SARS-CoV-2 infection of human ACE2-transgenic mice causes severe lung inflammation and impaired function. Nature Immunology 21(11):1327-1335, 2020.

48. Wu T., Hu E., Xu S., Chen M., Guo P., Dai Z., Feng T., Zhou L., Tang W., Zhan L., Fu X., Liu S., Bo X. and Yu G. clusterProfiler 4.0: A universal enrichment tool for interpreting omics data. The Innovation 2(3):100141, 2021.

49. Yamakita Y., Matsumura F., Lipscomb M.W., Chou P.-c., Werlen G., Burkhardt J.K. and Yamashiro S. Fascin1 Promotes Cell Migration of Mature Dendritic Cells. The Journal of Immunology 186(5):2850-2859, 2011.

50. Yu S., Zheng X., Zhou B., Li J., Chen M., Deng R., Wong G., Lavillette D. and Meng G. SARS-CoV-2

spike engagement of ACE2 primes S2′ site cleavage and fusion initiation. Proceedings of the National Academy of Sciences 119(1):e2111199119, 2022.

51. Zoufaly A., Poglitsch M., Aberle J.H., Hoepler W., Seitz T., Traugott M., Grieb A., Pawelka E., Laferl H., Wenisch C., Neuhold S., Haider D., Stiasny K., Bergthaler A., Puchhammer-Stoeckl E., Mirazimi A., Montserrat N., Zhang H., Slutsky A.S. and Penninger J.M. Human recombinant soluble ACE2 in severe COVID-19. The Lancet Respiratory Medicine 8(11):1154-1158, 2020.

FIGURE LEGENDS

Fig. 1 Enhanced sACE2-Fc with two single mutations exhibited broad-spectrum neutralization of SARS-CoV-2 variants. a Schematic representation of sACE2-Fc structure (upper) and neutralization assay setup (lower). Key amino acid positions (90-92 and 374-378) involved in glycosylation and zinc binding are highlighted. Red stars mark the positions of mutations in the sACE2-Fc mutant B5-D3. SP, signal peptide; CLD, collectrin-like domain; hIgG1, human IgG1. **b** Comparative bar graph showing the half-maximal inhibitory concentration (IC_{50}) values for neutralization of Wuhan-Hu-1 and D614G pseudovirues by WT sACE2-Fc and mutants (B2 to B6, A2, A3, D1 to D5, and B5-derivatives). The red arrow emphasizes the superior performance of the B5-D3 mutant. Enzymatic activity of each construct is plotted on the right axis. **c** List of pseudoviruses carrying spikes from different SARS-CoV-2 variants tested, categorized by the World Health Organization (WHO) into VOCs and VOIs. **d** Graph displaying IC_{50} values of WT sACE2-Fc, B5, and B5-D3/4/5 mutants against various SARS-CoV-2 VOCs and VOIs in neutralization assays. **e** Schematics of the plaque-reduction neutralization tests (PRNTs) process (upper) and the resulting IC_{50} values for B5-D3, Casirivimab, and hIgG1 against authentic SARS-CoV-2 (lower). **f, g** Dose-response curves depicting the neutralization efficacy of B5-D3 (orange), Casirivimab (purple), and hIgG1 (grey) in PRNTs against authentic SARS-CoV-2 Wuhan-Hu-1 and Delta strains (**f**), and Omicron sub-lineages (**g**). Data are presented as mean ± standard deviation (SD) from duplicate experiments.

831

832 **Fig. 2 Enhanced survival and reduced infection in K18-hACE2 mice through intranasal**
833 **prophylaxis with B5-D3 against SARS-CoV-2. a–e** Female K18-hACE2 mice, aged 10 to 12
834 months, were inoculated with 1×10^4 PFU of SARS-CoV-2 (Wuhan-Hu-1 strain). Mice were
835 treated with B5-D3 6 h prior (–6 h) via intranasal (IN, red) or intravenous (IV, green) routes, or
836 24 h post-infection (+24 h, blue) via IV (n = 5 each). IN PBS administered 6 h prior to viral
837 challenge served as the vehicle control (black; n = 5), and PBS alone was used for mock
838 control (grey; n = 4) (**a**). Body weight and survival were monitored over 14 days (**b**, **c**). One
839 mouse from each group was sacrificed at 4 dpi for analysis of viral titers in lung homogenates
840 using a median tissue culture infectious dose ($TCID_{50}$) assay (**d**). IHC staining for N protein
841 and H&E staining were performed on lung tissues collected at 4 dpi (**e**). Black arrows indicate
842 alveolar thickening, and yellow arrows show leukocyte infiltration. Scale bar = 100 μm. ND,
843 not detected; LOD, limit of detection. **f–i** Young female K18-hACE2 mice, aged 2 to 3 months,
844 were inoculated similarly and treated with B5-D3 via IN route at 24 h before (–24 h, pink), 6 h
845 before (–6 h, red), or 24 h after (+24 h, orange) the viral challenge (n = 5). Mice receiving IN
846 PBS 6 h before infection served as the vehicle control (black), with mock control mice
847 receiving PBS alone (grey) (**f**). Body weight (**g**) and survival (**h**) were recorded for 14 days.
848 Neutralizing antibody titers against Wuhan-Hu-1 in serum samples from surviving mice at 14
849 dpi were determined using Vero E6 cells (**i**). nAb, neutralizing antibody. Data are presented as
850 the geometric mean ± geometric SD. Statistical significance was determined using Dunn's
851 multiple comparisons test.

852

853 **Fig. 3 Efficient viral clearance at early stages through intranasal prophylaxis with B5-D3**
854 **against SARS-CoV-2 challenge in K18-hACE2 mice. a** Workflow diagram showing
855 timelines and treatments for different mouse groups. Young female K18-hACE2 mice aged 2 to
856 3 months received prophylactic administration of PBS (black), B5-D3 (red), or B5-D3-LALA
857 (purple) via the IN route 6 h prior to inoculation with 1×10^4 PFU of Wuhan-Hu-1. Mice
858 inoculated with PBS instead of the virus served as mock controls (grey). Mice from each
859 treatment group were sacrificed for tissue collection at 1, 2, and 4 dpi (n = 3 per time point). **b**
860 Quantitative PCR results showing relative amounts of *S* (upper) and *N* (lower) viral RNA in
861 lung tissues collected from different groups at 1, 2, and 4 dpi, normalized to mouse *Gapdh* (**a**).
862 **c** The titers of infectious viruses detected in lung homogenates, measured by $TCID_{50}$ assays at
863 1, 2, and 4 dpi. **d, e** Fixed lung tissues were sectioned and stained; IHC for viral N protein (**d**)
864 and H&E staining for tissue damage (**e**) are shown (scale bar = 100 μm). Data presented as
865 mean ± standard error of the mean (SEM). Statistical significance was determined by Tukey's
866 multiple comparisons test.
867
868
869 **Fig. 4 Transcriptomic analysis revealed early immune activation in IN B5-D3-prophylaxis**
870 **mouse group after SARS-CoV-2 challenge. a–d** DGE analysis comparing PBS (**a**), B5-D3
871 (**c**), and B5-D3-LALA (**d**) against the mock control at specific time points (n = 3). Volcano
872 plots illustrate the gene expression changes (**a**, **c**, **d**), while red and blue dots represent
873 significantly upregulated and downregulated genes, respectively, with $|\log_2$ fold change
874 $(\log_2 FC)| \geq 1$ and a false discovery rate (FDR) < 0.05. Bar chart in **b** shows the enrichment of
875 GOBP "response to virus" observed in PBS groups at 1, 2, 4 dpi, in which adjusted p values

are indicated for individual comparisons. **e**–**g** Comparison between IN B5-D3 and PBS group at 1 dpi. Volcano plot illustrates the DGE analysis between IN B5-D3 to PBS group at 1 dpi (**e**), with red and blue dots representing significantly upregulated and downregulated genes, respectively, with $|\log_2 FC| \geq 1$ and FDR < 0.05. GSEA shows top 15 significantly activated GOBPs (**f**) and KEGG pathways (**g**) in IN B5-D3 compared to PBS group at 1 dpi. NES, normalized enrichment score; p.adj, adjusted *p* value. **h**–**j** GSEA plots of chemotaxis (**h**), Rap1 signaling pathway (**i**), and Th1 and Th2 cell differentiation in B5-D3 vs PBS comparison at 1 dpi. **k**, **l** Heatmaps show NES of GSEA comparing various treatments to the mock control (**k**) and between B5-D3 to PBS (**l**), focusing on top 10 GOBPs highlighted in **f** and **Supplementary Figure 9c, d**, respectively, and those related to immune cell chemotaxis. Significant NES values ($p < 0.05$, FDR < 0.25) were highlighted in yellow. Benjamin–Hochberg method was used for FDR adjustment.

Fig. 5 *In vivo* bio-distribution of B5-D3 after IN administration. a Schematic workflow of *in vivo* and *ex vivo* imaging. Female K18-hACE2 mice aged 2 to 3 months received IN administration of fluorescently labeled B5-D3 (B5-D3-AF750) and was visualized at different time points. **b** Representative whole-body images of control and treated mice at 5 min, 1 h, and 24 h after B5-D3-AF750 administration, showing the signal captured by *in vivo* imaging (left). White circles indicate regions of interest (ROIs) for quantification of fluorescence signals in the nasal cavities. Average (Avg) Radiance measured at all time points are shown on the right. **c** *Ex vivo* images of tissues from control and treated mice sacrificed at indicated time points after B5-D3-AF750 administration. Blue circles indicate ROIs for signal quantification. Br, brain; NC, nasal cavity; T, trachea; Lu, lung; H, heart; Lv, liver; S, spleen; K, kidney; UB, urinary bladder; Bl, blood; Ur, urine. **d** Avg Radiance shows the fluorescence signals in excised tissues measured *ex vivo*. **e** Schematic workflow for BALF analysis. Female K18-hACE2 mice aged 2 to 3 months received IN administration of B5-D3-AF750 (n = 3) or PBS (n = 4) and

902 were sacrificed at 6 h later for collection of BALF cells. **f** Percentage of $CD45^+$ cells in live
903 BALF cells. **g** Positive rates (left) and histograms (right) of B5-D3 binding/uptake in $CD45^+$
904 BALF cells. Histograms show B5-D3-AF750 fluorescence intensities in $CD45^+$ BALF cells
905 from individual mice. **h** Frequency of individual immune cell types in $CD45^+$B5-$D3^+$ BALF
906 cells. Red arrows point out AM and Mono-Mac with high abundance. AM, alveolar
907 macrophage; Mono-Mac, monocyte-derived macrophage; cDC1/2, type 1 or 2 conventional
908 dendritic cells. **i**, **j** Positive rates (left) and histograms (right) of B5-D3 binding/uptake in
909 $CD11c^+$Siglec-F^+ AMs (**i**) and $CD11b^-$F4/80^+ mono-Macs (**j**). **k** Median fluorescence intensity
910 (MFI) of AF750 indicate B5-D3 binding/uptake in different $CD45^+$B5-$D3^+$ populations. **l**
911 Confocal images (scale bar = 50 μm) of BALF cells collected at 6 h and stained for sACE2-Fc
912 (red, Abcam, ab98596), Siglec-F (green, BD #564514), and nuclei (blue, Hoechst). Magnified
913 views are shown in white rectangles. Data are presented as mean ± SEM, and statistical
914 significance was determined by Tukey's multiple comparisons test or Student's t-test.

915

916 **Fig. 6 B5-D3 enhanced phagocytosis and degradation of SARS-CoV-2 pseudovirus in**
917 **THP-1-derived macrophages. a** Immunostaining of p24 (Invitrogen #PA5-81773), sACE2-Fc
918 (Abcam #ab98596), and LAMP1 (Abcam #ab25630) in THP-1-differentiated M0 macrophages
919 showing phagocytosis of SARS-CoV-2 pseudovirus ($p24^+$) after 6 h of incubation with or
920 without sACE2-Fc (scale bar = 50 μm). LAMP1 was stained to identify lysosomes. **b**
921 Quantification of p24 signal intensity as shown in **a**. Intensity Density (IntDen) per cell number
922 indicates the mean p24 signal per cell, calculated using ImageJ. Each dot represents one image.
923 **c** Manders' coefficient indicating the colocalization of p24 and LAMP1 in THP-1 M0
924 macrophages as shown in **a**. **d** Immunostaining of p24, sACE2-Fc, and LAMP1 in hACE2-
925 Calu-3 cells after 6 h incubation with pseudovirus, with or without B5-D3 (scale bar = 50 μm).
926 **e** Quantification of mean p24 signal intensity as shown in **d**. **f** Manders' coefficient for the

927 colocalization of p24 and LAMP1 in hACE2-Calu-3 cells, as shown in **d**. **g** Quantification of
928 pseudovirus infection in THP-1, M0 macrophages, M1 macrophages, hACE2-Calu-3, and
929 hACE2-293T cells, in the presence or absence of sACE2-Fc. Results shown were luciferase
930 activities measured at 2 days post-transduction. **h** Immunoblot staining to detect SARS-CoV-2
931 spike cleavage after cell entry. M0 macrophages, M1 macrophages, and hACE2-293T cells
932 were incubated with pseudovirus for 6 h, with or without sACE2-Fc, before protein extraction.
933 Data are presented as mean ± SEM, and statistical significance was determined by Tukey's
934 multiple comparisons test.

935

936 **Fig. 7 Proposed mechanisms of action of IN sACE2-Fc decoy in preventing SARS-CoV-2**
937 **infection. a, b** Schematics illustrating the actions and outcomes of SARS-CoV-2 infection, in
938 the absence (**a**) and presence (**b**) of IN delivered sACE2-Fc decoys. The figure was generated
939 in Biorender.

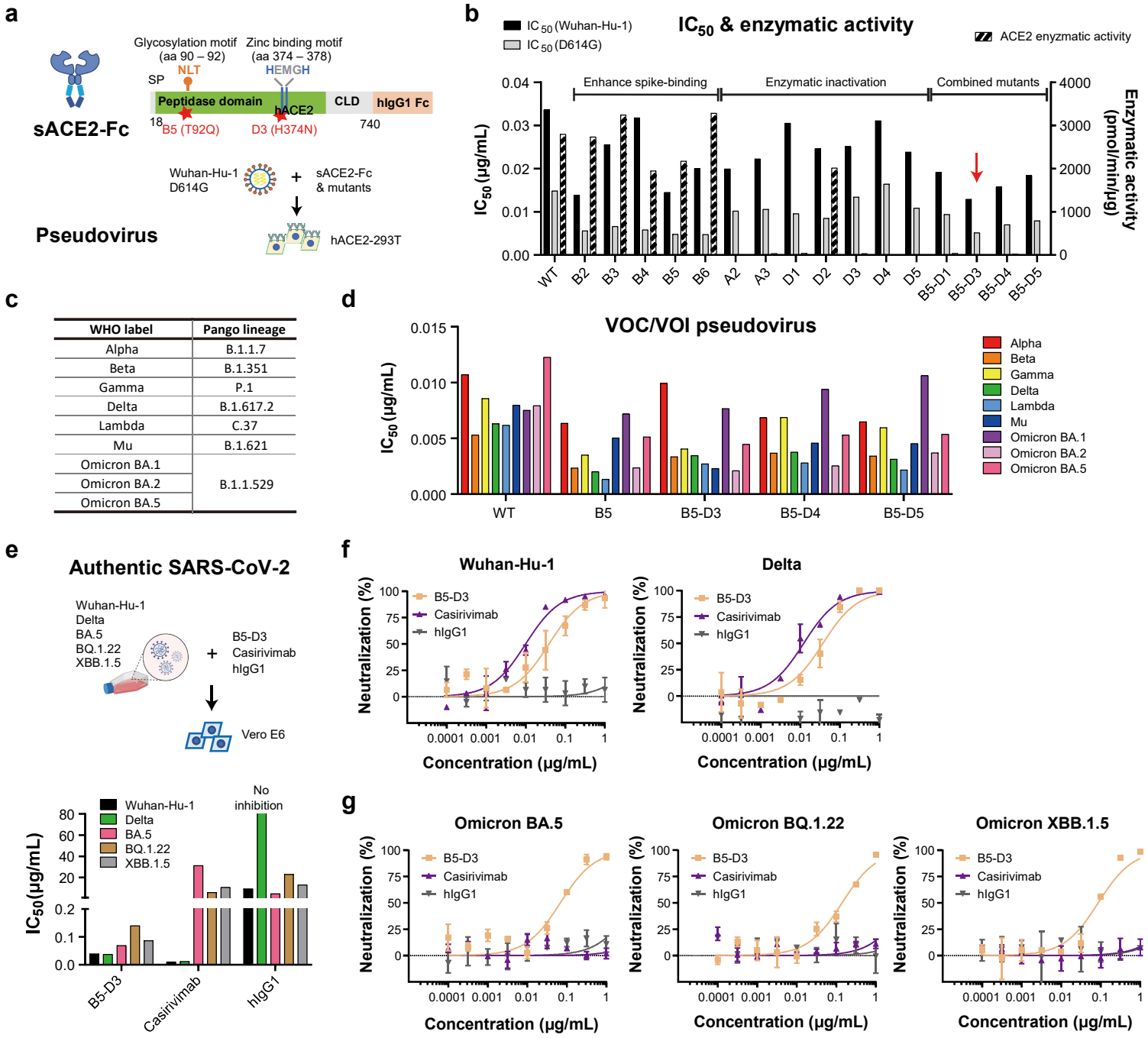
a
sACE2-Fc
Glycosylation motif (aa 90 – 92)
Zinc binding motif (aa 374 – 378)
NLT
HEMGH
SP
Peptidase domain
hACE2
CLD
hIgG1 Fc
18
740
B5 (T92Q)
D3 (H374N)
Pseudovirus
Wuhan-Hu-1 D614G
sACE2-Fc & mutants
hACE2-293T
b
IC50 (Wuhan-Hu-1)
IC50 (D614G)
IC50 & enzymatic activity
ACE2 enyzmatic activity
Enhance spike-binding
Enzymatic inactivation
Combined mutants
IC50 (μg/mL)
Enzymatic activity (pmol/min/μg)
WT
B2
B3
B4
B5
B6
A2
A3
D1
D2
D3
D4
D5
B5-D1
B5-D3
B5-D4
B5-D5
c
WHO label
Pango lineage
Alpha
B.1.1.7
Beta
B.1.351
Gamma
P.1
Delta
B.1.617.2
Lambda
C.37
Mu
B.1.621
Omicron BA.1
Omicron BA.2
Omicron BA.5
B.1.1.529
d
VOC/VOI pseudovirus
IC50 (μg/mL)
Alpha
Beta
Gamma
Delta
Lambda
Mu
Omicron BA.1
Omicron BA.2
Omicron BA.5
WT
B5
B5-D3
B5-D4
B5-D5
e
Authentic SARS-CoV-2
Wuhan-Hu-1
Delta
BA.5
BQ.1.22
XBB.1.5
B5-D3
Casirivimab
hIgG1
Vero E6
IC50(μg/mL)
Wuhan-Hu-1
Delta
BA.5
BQ.1.22
XBB.1.5
No inhibition
B5-D3
Casirivimab
hIgG1
f
Wuhan-Hu-1
Delta
Neutralization (%)
B5-D3
Casirivimab
hIgG1
Concentration (μg/mL)
g
Omicron BA.5
Omicron BQ.1.22
Omicron XBB.1.5
Neutralization (%)
B5-D3
Casirivimab
hIgG1
Concentration (μg/mL)

Figure 1

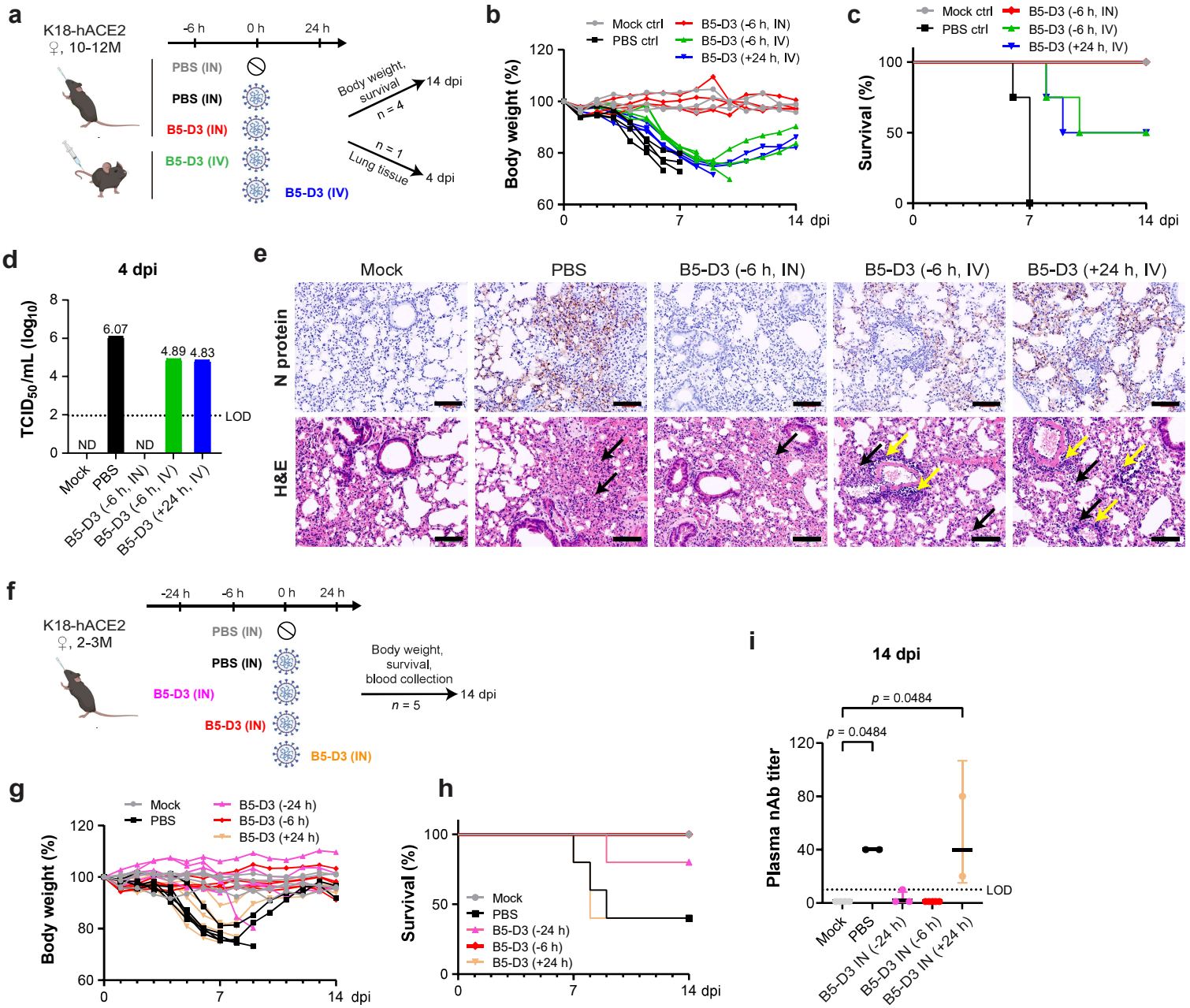
a
K18-hACE2
♀, 10-12M
-6 h
0 h
24 h
PBS (IN)
PBS (IN)
B5-D3 (IN)
B5-D3 (IV)
B5-D3 (IV)
Body weight, survival
n = 4
14 dpi
n = 1
Lung tissue
4 dpi
b
Mock ctrl
PBS ctrl
B5-D3 (-6 h, IN)
B5-D3 (-6 h, IV)
B5-D3 (+24 h, IV)
Body weight (%)
14 dpi
c
Survival (%)
14 dpi
d
4 dpi
TCID50/mL (log10)
6.07
4.89
4.83
ND
ND
LOD
Mock
PBS
B5-D3 (-6 h, IN)
B5-D3 (-6 h, IV)
B5-D3 (+24 h, IV)
e
Mock
PBS
B5-D3 (-6 h, IN)
B5-D3 (-6 h, IV)
B5-D3 (+24 h, IV)
N protein
H&E
f
K18-hACE2
♀, 2-3M
-24 h
-6 h
0 h
24 h
PBS (IN)
PBS (IN)
B5-D3 (IN)
B5-D3 (IN)
B5-D3 (IN)
Body weight, survival, blood collection
n = 5
14 dpi
g
Mock
PBS
B5-D3 (-24 h)
B5-D3 (-6 h)
B5-D3 (+24 h)
Body weight (%)
14 dpi
h
Survival (%)
Mock
PBS
B5-D3 (-24 h)
B5-D3 (-6 h)
B5-D3 (+24 h)
14 dpi
i
14 dpi
p = 0.0484
p = 0.0484
Plasma nAb titer
LOD
Mock
PBS
B5-D3 IN (-24 h)
B5-D3 IN (-6 h)
B5-D3 IN (+24 h)

Figure 2

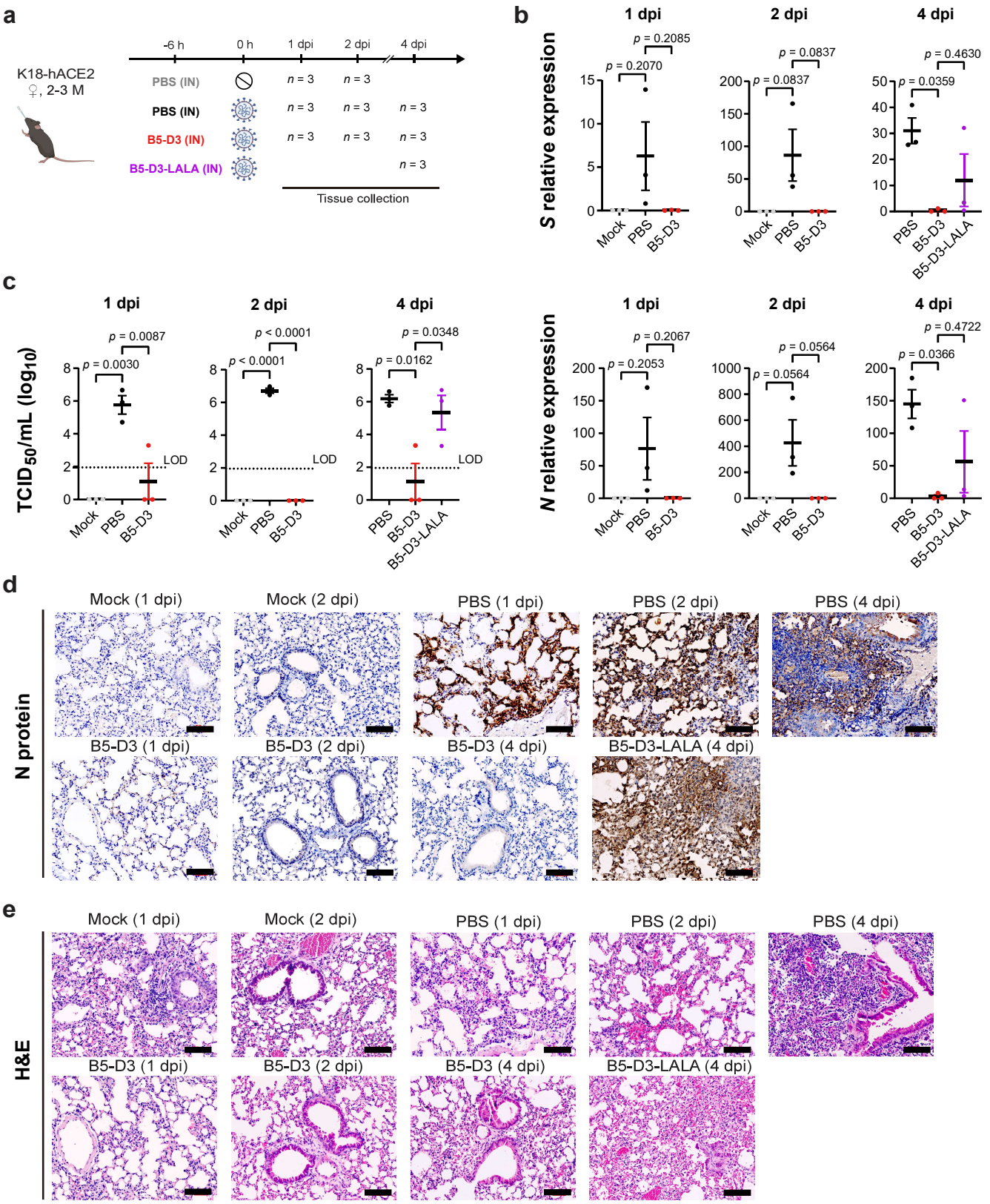
a
K18-hACE2
♀, 2-3 M
-6 h
0 h
1 dpi
2 dpi
4 dpi
PBS (IN)
PBS (IN)
B5-D3 (IN)
B5-D3-LALA (IN)
n = 3
Tissue collection
b
1 dpi
2 dpi
4 dpi
S relative expression
p = 0.2085
p = 0.2070
p = 0.0837
p = 0.0837
p = 0.4630
p = 0.0359
Mock
PBS
B5-D3
B5-D3-LALA
c
TCID50/mL (log10)
p = 0.0087
p = 0.0030
p < 0.0001
p < 0.0001
p = 0.0348
p = 0.0162
LOD
N relative expression
p = 0.2067
p = 0.2053
p = 0.0564
p = 0.0564
p = 0.4722
p = 0.0366
d
N protein
Mock (1 dpi)
Mock (2 dpi)
PBS (1 dpi)
PBS (2 dpi)
PBS (4 dpi)
B5-D3 (1 dpi)
B5-D3 (2 dpi)
B5-D3 (4 dpi)
B5-D3-LALA (4 dpi)
e
H&E
Mock (1 dpi)
Mock (2 dpi)
PBS (1 dpi)
PBS (2 dpi)
PBS (4 dpi)
B5-D3 (1 dpi)
B5-D3 (2 dpi)
B5-D3 (4 dpi)
B5-D3-LALA (4 dpi)

Figure 3

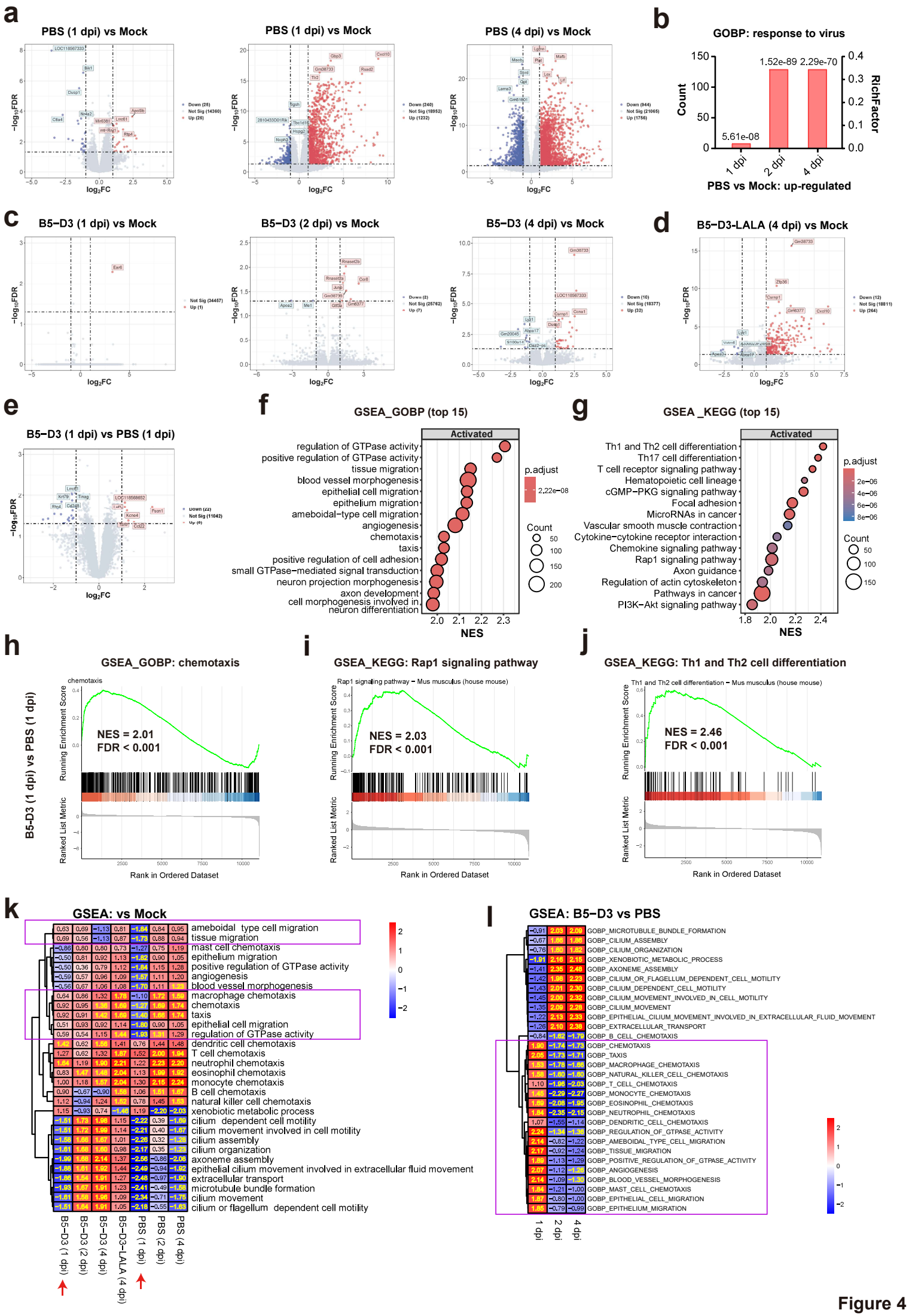
a
PBS (1 dpi) vs Mock
PBS (1 dpi) vs Mock
PBS (4 dpi) vs Mock
−log10FDR
log2FC
Down (25)
Not Sig (14360)
Up (26)
Down (240)
Not Sig (18952)
Up (1232)
Down (944)
Not Sig (21065)
Up (1756)
b
GOBP: response to virus
Count
RichFactor
5.61e-08
1.52e-89
2.29e-70
1 dpi
2 dpi
4 dpi
PBS vs Mock: up-regulated
c
B5−D3 (1 dpi) vs Mock
B5−D3 (2 dpi) vs Mock
B5−D3 (4 dpi) vs Mock
Not Sig (34457)
Up (1)
Down (2)
Not Sig (25762)
Up (7)
Down (10)
Not Sig (18377)
Up (32)
d
B5−D3-LALA (4 dpi) vs Mock
Down (12)
Not Sig (18811)
Up (264)
e
B5−D3 (1 dpi) vs PBS (1 dpi)
Down (22)
Not Sig (11042)
Up (0)
f
GSEA_GOBP (top 15)
Activated
regulation of GTPase activity
positive regulation of GTPase activity
tissue migration
blood vessel morphogenesis
epithelial cell migration
epithelium migration
ameboidal−type cell migration
angiogenesis
chemotaxis
taxis
positive regulation of cell adhesion
small GTPase−mediated signal transduction
neuron projection morphogenesis
axon development
cell morphogenesis involved in neuron differentiation
p.adjust
2.22e−08
Count
NES
g
GSEA _KEGG (top 15)
Activated
Th1 and Th2 cell differentiation
Th17 cell differentiation
T cell receptor signaling pathway
Hematopoietic cell lineage
cGMP−PKG signaling pathway
Focal adhesion
MicroRNAs in cancer
Vascular smooth muscle contraction
Cytokine−cytokine receptor interaction
Chemokine signaling pathway
Rap1 signaling pathway
Axon guidance
Regulation of actin cytoskeleton
Pathways in cancer
PI3K−Akt signaling pathway
p.adjust
Count
NES
h
GSEA_GOBP: chemotaxis
B5-D3 (1 dpi) vs PBS (1 dpi)
chemotaxis
NES = 2.01
FDR < 0.001
Running Enrichment Score
Ranked List Metric
Rank in Ordered Dataset
i
GSEA_KEGG: Rap1 signaling pathway
Rap1 signaling pathway − Mus musculus (house mouse)
NES = 2.03
FDR < 0.001
Running Enrichment Score
Ranked List Metric
Rank in Ordered Dataset
j
GSEA_KEGG: Th1 and Th2 cell differentiation
Th1 and Th2 cell differentiation − Mus musculus (house mouse)
NES = 2.46
FDR < 0.001
Running Enrichment Score
Ranked List Metric
Rank in Ordered Dataset
k
GSEA: vs Mock
ameboidal type cell migration
tissue migration
mast cell chemotaxis
epithelium migration
positive regulation of GTPase activity
angiogenesis
blood vessel morphogenesis
macrophage chemotaxis
chemotaxis
taxis
epithelial cell migration
regulation of GTPase activity
dendritic cell chemotaxis
T cell chemotaxis
neutrophil chemotaxis
eosinophil chemotaxis
monocyte chemotaxis
B cell chemotaxis
natural killer cell chemotaxis
xenobiotic metabolic process
cilium dependent cell motility
cilium movement involved in cell motility
cilium assembly
cilium organization
axoneme assembly
epithelial cilium movement involved in extracellular fluid movement
extracellular transport
microtubule bundle formation
cilium movement
cilium or flagellum dependent cell motility
B5−D3 (1 dpi)
B5−D3 (2 dpi)
B5−D3 (4 dpi)
B5−D3−LALA (4 dpi)
PBS (1 dpi)
PBS (2 dpi)
PBS (4 dpi)
l
GSEA: B5−D3 vs PBS
GOBP_MICROTUBULE_BUNDLE_FORMATION
GOBP_CILIUM_ASSEMBLY
GOBP_CILIUM_ORGANIZATION
GOBP_XENOBIOTIC_METABOLIC_PROCESS
GOBP_AXONEME_ASSEMBLY
GOBP_CILIUM_OR_FLAGELLUM_DEPENDENT_CELL_MOTILITY
GOBP_CILIUM_DEPENDENT_CELL_MOTILITY
GOBP_CILIUM_MOVEMENT_INVOLVED_IN_CELL_MOTILITY
GOBP_CILIUM_MOVEMENT
GOBP_EPITHELIAL_CILIUM_MOVEMENT_INVOLVED_IN_EXTRACELLULAR_FLUID_MOVEMENT
GOBP_EXTRACELLULAR_TRANSPORT
GOBP_B_CELL_CHEMOTAXIS
GOBP_CHEMOTAXIS
GOBP_TAXIS
GOBP_MACROPHAGE_CHEMOTAXIS
GOBP_NATURAL_KILLER_CELL_CHEMOTAXIS
GOBP_T_CELL_CHEMOTAXIS
GOBP_MONOCYTE_CHEMOTAXIS
GOBP_EOSINOPHIL_CHEMOTAXIS
GOBP_NEUTROPHIL_CHEMOTAXIS
GOBP_DENDRITIC_CELL_CHEMOTAXIS
GOBP_REGULATION_OF_GTPASE_ACTIVITY
GOBP_AMEBOIDAL_TYPE_CELL_MIGRATION
GOBP_TISSUE_MIGRATION
GOBP_POSITIVE_REGULATION_OF_GTPASE_ACTIVITY
GOBP_ANGIOGENESIS
GOBP_BLOOD_VESSEL_MORPHOGENESIS
GOBP_MAST_CELL_CHEMOTAXIS
GOBP_EPITHELIAL_CELL_MIGRATION
GOBP_EPITHELIUM_MIGRATION
1 dpi
2 dpi
4 dpi

Figure 4

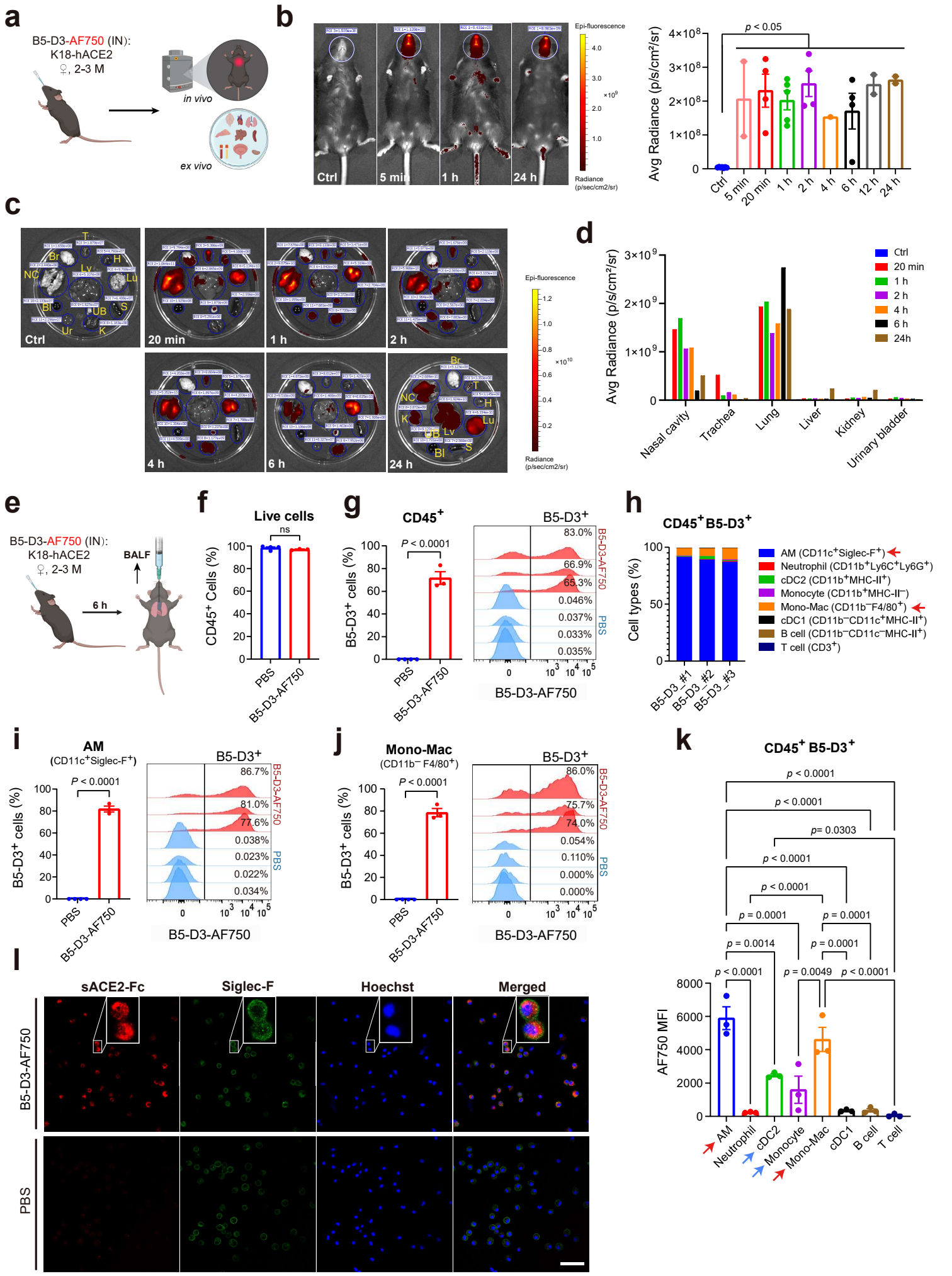
a
B5-D3-AF750 (IN):
K18-hACE2
♀, 2-3 M
in vivo
ex vivo
b
Ctrl
5 min
1 h
24 h
Epi-fluorescence
Radiance (p/sec/cm2/sr)
Avg Radiance (p/s/cm²/sr)
p < 0.05
Ctrl
5 min
20 min
1 h
2 h
4 h
6 h
12 h
24 h
c
Ctrl
20 min
1 h
2 h
4 h
6 h
24 h
Epi-fluorescence
Radiance (p/sec/cm2/sr)
d
Avg Radiance (p/s/cm²/sr)
Ctrl
20 min
1 h
2 h
4 h
6 h
24h
Nasal cavity
Trachea
Lung
Liver
Kidney
Urinary bladder
e
B5-D3-AF750 (IN):
K18-hACE2
♀, 2-3 M
6 h
BALF
f
Live cells
ns
CD45⁺ Cells (%)
PBS
B5-D3-AF750
g
CD45⁺
P < 0.0001
B5-D3⁺ cells (%)
B5-D3⁺
83.0%
66.9%
65.3%
0.046%
0.037%
0.033%
0.035%
B5-D3-AF750
PBS
B5-D3-AF750
h
CD45⁺ B5-D3⁺
Cell types (%)
AM (CD11c⁺Siglec-F⁺)
Neutrophil (CD11b⁺Ly6C⁺Ly6G⁺)
cDC2 (CD11b⁺MHC-II⁺)
Monocyte (CD11b⁺MHC-II⁻)
Mono-Mac (CD11b⁻F4/80⁺)
cDC1 (CD11b⁻CD11c⁺MHC-II⁺)
B cell (CD11b⁻CD11c⁻MHC-II⁺)
T cell (CD3⁺)
B5-D3_#1
B5-D3_#2
B5-D3_#3
i
AM
(CD11c⁺Siglec-F⁺)
P < 0.0001
B5-D3⁺ cells (%)
B5-D3⁺
86.7%
81.0%
77.6%
0.038%
0.023%
0.022%
0.034%
B5-D3-AF750
PBS
B5-D3-AF750
j
Mono-Mac
(CD11b⁻ F4/80⁺)
P < 0.0001
B5-D3⁺ cells (%)
B5-D3⁺
86.0%
75.7%
74.0%
0.054%
0.110%
0.000%
0.000%
B5-D3-AF750
PBS
B5-D3-AF750
k
CD45⁺ B5-D3⁺
p < 0.0001
p < 0.0001
p= 0.0303
p < 0.0001
p < 0.0001
p = 0.0001
p = 0.0001
p = 0.0014
p = 0.0001
p < 0.0001
p = 0.0049
p < 0.0001
AF750 MFI
AM
Neutrophil
cDC2
Monocyte
Mono-Mac
cDC1
B cell
T cell
l
sACE2-Fc
Siglec-F
Hoechst
Merged
B5-D3-AF750
PBS

Figure 5

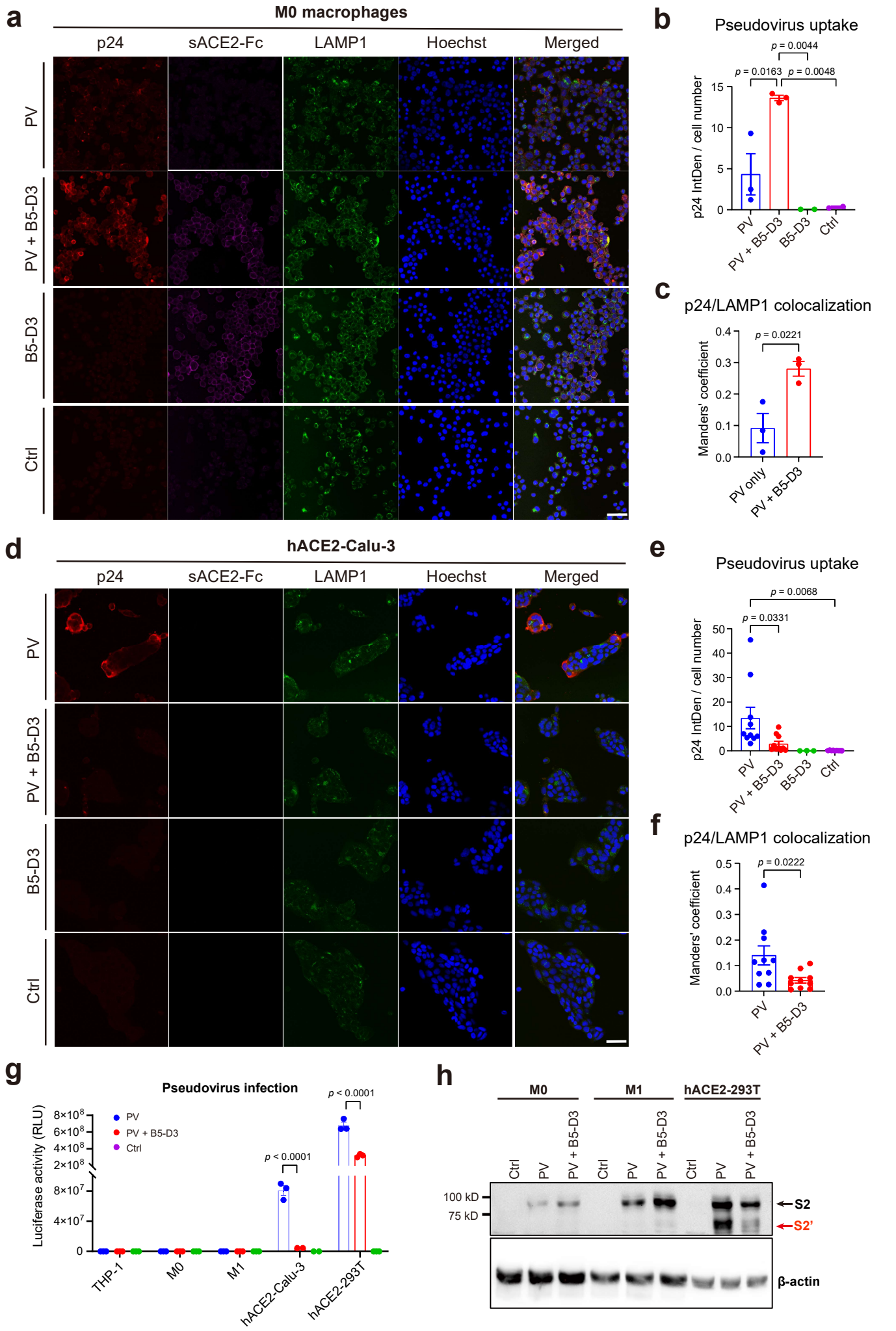
a
M0 macrophages
p24
sACE2-Fc
LAMP1
Hoechst
Merged
PV
PV + B5-D3
B5-D3
Ctrl
b
Pseudovirus uptake
p = 0.0044
p = 0.0163
p = 0.0048
p24 IntDen / cell number
PV
PV + B5-D3
B5-D3
Ctrl
c
p24/LAMP1 colocalization
p = 0.0221
Manders' coefficient
PV only
PV + B5-D3
d
hACE2-Calu-3
p24
sACE2-Fc
LAMP1
Hoechst
Merged
PV
PV + B5-D3
B5-D3
Ctrl
e
Pseudovirus uptake
p = 0.0068
p = 0.0331
p24 IntDen / cell number
PV
PV + B5-D3
B5-D3
Ctrl
f
p24/LAMP1 colocalization
p = 0.0222
Manders' coefficient
PV
PV + B5-D3
g
Pseudovirus infection
Luciferase activity (RLU)
PV
PV + B5-D3
Ctrl
p < 0.0001
p < 0.0001
THP-1
M0
M1
hACE2-Calu-3
hACE2-293T
h
M0
M1
hACE2-293T
Ctrl
PV
PV + B5-D3
100 kD
75 kD
S2
S2'
β-actin

Figure 6

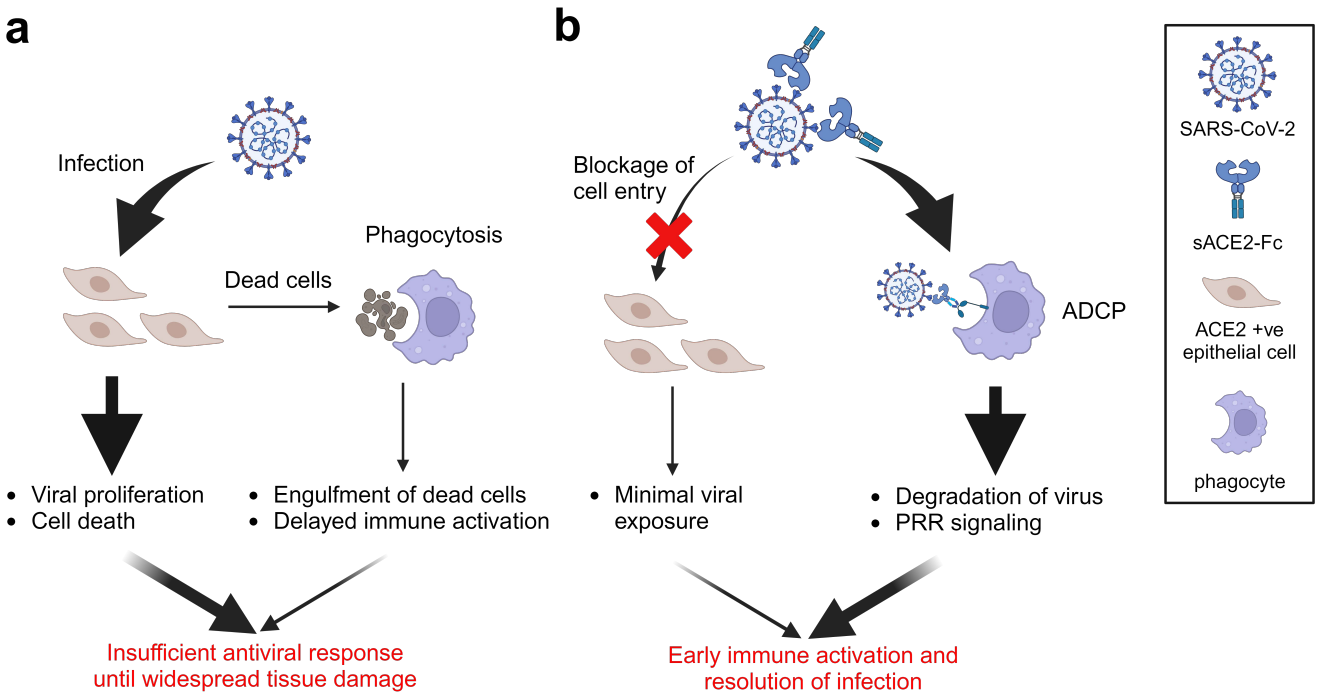
a
Infection
Dead cells
Phagocytosis
• Viral proliferation
• Cell death
• Engulfment of dead cells
• Delayed immune activation
Insufficient antiviral response
until widespread tissue damage
b
Blockage of
cell entry
ADCP
• Minimal viral
exposure
• Degradation of virus
• PRR signaling
Early immune activation and
resolution of infection
SARS-CoV-2
sACE2-Fc
ACE2 +ve
epithelial cell
phagocyte

Figure 7